

Markerless 6D Pose Estimation and Position-Based Visual Servoing for Endoscopic Continuum Manipulators

Junhyun Park*, Chunggil An*, Myeongbo Park, Ihsan Ullah, Sihyeong Park, and Minho Hwang[†]

Abstract—Continuum manipulators in flexible endoscopic surgical systems offer high dexterity for minimally invasive procedures; however, accurate pose estimation and closed-loop control remain challenging due to hysteresis, compliance, and limited distal sensing. Vision-based approaches reduce hardware complexity but are often constrained by limited geometric observability and high computational overhead, restricting real-time closed-loop applicability. This paper presents a unified framework for markerless stereo 6D pose estimation and position-based visual servoing of continuum manipulators. A photo-realistic simulation pipeline enables large-scale automatic training with pixel-accurate annotations. A stereo-aware multi-feature fusion network jointly exploits segmentation masks, keypoints, heatmaps, and bounding boxes to enhance geometric observability. To enforce geometric consistency without iterative optimization, a feed-forward rendering-based refinement module predicts residual pose corrections in a single pass. A self-supervised sim-to-real adaptation strategy further improves real-world performance using unlabeled data. Extensive real-world validation achieves a mean translation error of 0.83 mm and a mean rotation error of 2.76° across 1,000 samples. Markerless closed-loop visual servoing driven by the estimated pose attains accurate trajectory tracking with a mean translation error of 2.07 mm and a mean rotation error of 7.41°, corresponding to 85% and 59% reductions compared to open-loop control, together with high repeatability in repeated point-reaching tasks. To the best of our knowledge, this work presents the first fully markerless pose-estimation-driven position-based visual servoing framework for continuum manipulators, enabling precise closed-loop control without physical markers or embedded sensing.

I. INTRODUCTION

Flexible endoscopic surgical systems enable minimally invasive access to complex anatomical pathways via natural orifices (e.g., gastrointestinal or transoral routes). Unlike rigid laparoscopic robots, these platforms rely on continuum manipulators capable of large deformation and high dexterity, which have attracted increasing research attention in recent years [1]–[5].

Accurate pose estimation and control are fundamental requirements in robotic surgical systems. However, in cable-driven continuum manipulators, precise control remains particularly challenging due to friction, backlash, torsion, cable elongation, structural compliance, and strong inter-channel coupling along long tendon-sheath transmission paths [6]–[10]. Unlike rigid-link robots, where joint encoders directly

measure each articulated degree of freedom and enable reliable forward kinematics, continuum manipulators cannot accommodate distributed sensing along their flexible backbone due to size constraints and mechanical complexity. Furthermore, long transmission distances—often exceeding one meter—introduce significant hysteresis and nonlinearities, rendering motor-side measurements insufficient for accurately recovering distal tool configuration.

To mitigate these limitations, external sensing modalities such as fiber Bragg grating (FBG) sensors and electromagnetic (EM) tracking systems have been investigated to directly measure tool shape or pose [11], [12]. While accurate, these approaches require additional hardware integration, increasing system complexity and limiting clinical practicality. FBG-based systems are sensitive to mechanical fatigue and require costly interrogation and calibration procedures, whereas EM tracking is susceptible to metallic interference commonly present in surgical environments.

In contrast, cameras are already integrated into many surgical platforms to provide visual perception for both surgeons and robotic systems [1]–[4], [13]. Recent learning-based approaches have shown promising progress in markerless surgical tool pose estimation [14]–[19]. However, most existing methods predominantly rely on monocular imagery and single-modality visual cues—such as keypoints or segmentation masks alone—resulting in insufficient geometric constraints for accurate 6D pose recovery, particularly under depth ambiguity.

Moreover, learning-based pose estimation critically depends on large-scale datasets with reliable ground-truth annotations. However, acquiring accurate 6D pose labels for continuum manipulators in real surgical environments is inherently challenging. Prior efforts have relied on manual annotation [20], [21], heuristic or color-based segmentation [16], or CAD-based rendering pipelines that lack physics-consistent motion modeling and photo-realistic appearance [15]. These strategies limit annotation scalability and often introduce label noise, resulting in geometric inconsistencies and an increased sim-to-real domain gap.

Most existing approaches directly regress 6D pose from visual observations in a feed-forward manner. However, such predictions do not explicitly enforce geometric consistency between the estimated pose and the observed image evidence, often resulting in sub millimeter-level errors in real surgical scenes [17], [22]. These inaccuracies are particularly detrimental in closed-loop robotic control, where small pose deviations can accumulate and degrade control stability. To improve geometric alignment, iterative render-and-compare

*These authors contributed equally. [†]Corresponding author.

All authors are with the Department of Robotics and Mechatronics Engineering, Daegu Gyeongbuk Institute of Science and Technology (DGIST), Daegu 42988, Republic of Korea. (e-mail: junhyunpark0507@gmail.com, {cndrlfwlq, qkraudqh23, ihsankhan, psh120, minho}@dgist.ac.kr).

refinement methods have been introduced to minimize visual reprojection errors [15]. While effective in reducing pose error, their reliance on repeated rendering and optimization incurs substantial computational overhead, which limits real-time deployment in control-critical applications.

Beyond pose estimation, reliable closed-loop control is essential for autonomous surgical manipulation. Existing visual servoing approaches for continuum manipulators have primarily relied on position-based visual servoing (PBVS) using external markers to obtain accurate tool pose [23], or image-based visual servoing (IBVS) that directly maps image discrepancies to control commands without explicit pose estimation [24]. While marker-based PBVS provides precise geometric feedback, it is impractical in realistic surgical environments, whereas IBVS is tightly coupled to target appearance and lacks explicit task-space pose representation, limiting generalization across varying surgical scenarios. Consequently, closed-loop control of continuum manipulators using markerless, geometrically consistent task-space pose estimation remains largely unexplored.

To address these challenges, we present a unified markerless position-based visual servoing framework that directly estimates geometrically consistent 6D task-space pose from stereo image observations and enables real-time closed-loop control of continuum manipulators without external markers or embedded sensing hardware.

- **Physics-grounded photo-realistic synthetic data generation:** We develop a high-fidelity simulation pipeline for large-scale continuum manipulator data generation, enabling physically plausible motion under kinematic constraints with pixel-accurate 6D pose annotations.
- **Multi-feature stereo pose estimation with feed-forward rendering refinement:** We propose a stereo-aware multi-feature fusion framework that jointly integrates segmentation masks, keypoints, heatmaps, and bounding boxes to estimate 6D pose. A feed-forward rendering-based refinement module predicts residual pose corrections in a single forward pass (87 ms), achieving state-of-the-art real-world accuracy while reducing computation by an order of magnitude compared to iterative render-and-compare methods [15], [16].
- **Self-supervised sim-to-real adaptation without manual labels:** We introduce a pseudo ground-truth refinement strategy to mitigate calibration errors and domain shift, reducing real-world pose error by approximately 50% using only 150 unlabeled images.
- **Markerless position-based closed-loop visual servoing:** We demonstrate, for the first time, accurate closed-loop control of a continuum manipulator using purely vision-based estimated 6D task-space pose feedback, enabling markerless position-based visual servoing with a mean trajectory tracking error of 2.07 mm in translation and 7.41° in rotation, together with high repeatability in repeated point-reaching tasks.

II. RELATED WORKS

This section reviews prior studies in four aspects closely related to the proposed framework: vision-based pose estimation of continuum manipulators, synthetic data generation, rendering-based geometric refinement, and closed-loop visual control.

A. Pose Estimation of Continuum Manipulators

Pose estimation of continuum manipulators has predominantly relied on embedded sensing technologies. FBG sensors enable curvature reconstruction from distributed strain measurements [12], [25], while EM tracking systems directly localize the distal tip pose using externally tracked sensor coils [26]. Although these approaches provide high accuracy, they require dedicated hardware integration and increase overall system complexity.

To reduce dependence on specialized sensing hardware, markerless vision-based approaches have gained increasing attention. Existing methods typically extract a single geometric representation, including RANSAC-based shaft line tracking [19], Random Forest-based segmentation [16], convolutional-network-based mask estimation [15], [18], and keypoint-based pose regression [17]. While these approaches enable pose estimation from visual observations, they generally exploit only one type of visual cue and predominantly rely on monocular imagery.

Such formulations inherently limit geometric observability for full 6-DoF pose estimation. Specifically, monocular single-cue approaches are subject to scale and depth ambiguity, rendering accurate recovery of the translational component along the viewing direction ill-conditioned.

B. Synthetic Data Generation for Continuum Manipulators

Simulation-driven data generation has been widely adopted to enable scalable learning with accurate ground-truth supervision across diverse robotic platforms. ORBIT integrates physics-based simulation with photo-realistic rendering to automatically generate large-scale annotated datasets for articulated robots [27], while ORBIT-Surgical extends this paradigm to surgical robotics, providing scalable simulation and automatic annotation for learning-based manipulation [28].

In learning-based pose estimation for continuum manipulators, acquiring large-scale 6-DoF ground truth remains a major challenge. Existing approaches rely on external tracking systems, heuristic geometric estimation, or manual annotation [20], [21], as well as CAD-based pipelines that lack physically plausible motion modeling and photo-realistic rendering [15], [16]. These methods are inherently constrained by sensing noise, calibration errors, and limited scalability.

To address this gap, we discretize continuum deformation using a pseudo-rigid-body representation and construct a URDF-based physics simulation that enables automatic generation of physically plausible motion under rigid-body constraints together with pixel-accurate pose annotations for large-scale learning.

C. Differentiable Rendering-Based Pose Estimation

Differentiable rendering enables gradient-based pose refinement by measuring discrepancies between rendered geometric models and observed images in a differentiable manner. In robotics, it has been successfully applied to camera–robot extrinsic calibration and pose estimation by minimizing photometric or silhouette-based discrepancies between rendered predictions and observations [15], [16], [29]–[31]. Such approaches leverage explicit geometric alignment to achieve improved accuracy and robustness.

For extrinsic calibration, which is typically performed offline, the computational overhead of iterative rendering and optimization is acceptable. However, in pose estimation for closed-loop control, particularly position-based visual servoing, low-latency inference is essential to maintain control responsiveness and stability. Existing render-and-refine methods rely on repeated rendering and iterative updates, resulting in significant computational latency that limits their real-time applicability.

To address this limitation, we propose a feed-forward rendering-based refinement module that preserves geometric consistency while eliminating iterative optimization. Instead of performing gradient-based pose updates, our method directly predicts residual pose corrections from rendering discrepancies in a single forward pass, enabling efficient pose estimation suitable for closed-loop control.

D. Closed-Loop Control of Continuum Manipulators

Beyond marker-based visual tracking, numerous studies have focused on improving closed-loop control accuracy by leveraging model-based and model-free control strategies. Model-based approaches integrate analytical kinematics or Cosserat-rod models to continuously update robot states or Jacobians using sensor feedback [32]. Model-free methods, including Jacobian-free control laws and reinforcement learning-based controllers, further reduce reliance on explicit modeling [33], [34]. While effective in enhancing control performance under uncertainty, these methods assume reliable state measurements obtained from dedicated sensors or external tracking systems rather than direct pose estimation from image observations.

In markerless environments, existing vision-based control methods primarily adopt image-based visual servoing (IBVS) paradigms, where control commands are inferred directly from image feature discrepancies without explicit pose estimation [24]. While effective for reaching a predefined target image configuration, such approaches are inherently tied to target appearance and lack explicit task-space geometric feedback, which limits generalization across varying objects, viewpoints, and task conditions compared to position-based control frameworks.

III. HARDWARE AND KINEMATICS

We adopt a continuum manipulator design previously reported in [5], [10] as the experimental platform for pose

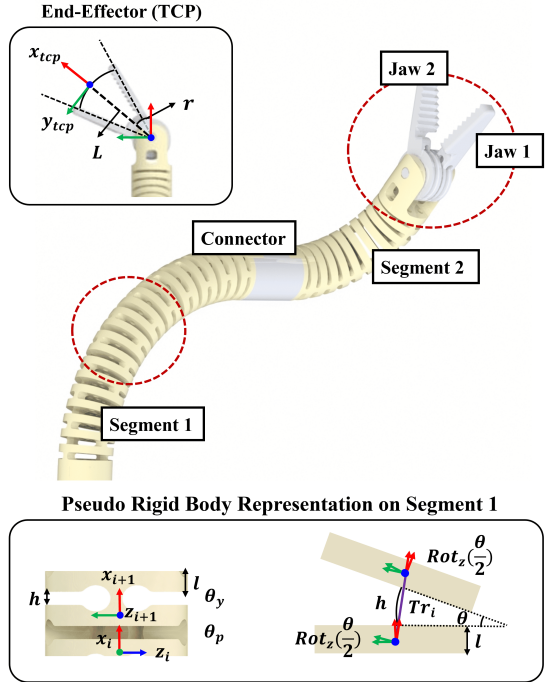


Fig. 1: Pseudo-rigid-body (PRB) kinematic model of the two-segment continuum manipulator. The system consists of two flexible segments, a rigid connector, and a dual-jaw gripper, where each flexible segment is discretized into revolute joints and rigid links. The first segment enables pitch–yaw bending, the second provides pitch bending, and the tool center point (TCP) is defined by the jaw geometry with associated yaw variable r .

estimation and control. This section summarizes the mechanical architecture and kinematic formulation, which form the basis for URDF construction and closed-loop visual servoing.

The manipulator consists of two flexible segments, a gripper hinge, and a dual-jaw gripper mounted on a central shaft (see Fig. 1), resulting in seven degrees of freedom (DoFs). The first two DoFs correspond to axial translation q_1 and global axial rotation q_2 of the entire structure. The first flexible segment enables bending in pitch and yaw, parameterized by q_3 and q_4 , respectively, whereas the second segment provides single-plane pitch bending q_5 . The gripper includes two independently actuated yaw joints q_6 and q_7 . The tool center point (TCP) is defined as the geometric midpoint of the circular arc formed by the jaw endpoints during symmetric yaw motion.

A. Forward Kinematics

The continuum structure is modeled using a pseudo-rigid-body (PRB) discretization, where each flexible segment is approximated by a sequence of revolute joints and rigid links. For the first segment, orthogonal bending in pitch and yaw is represented by alternating PRB modules. The homogeneous transformation of a single PRB module is given by

$$\mathbf{T}_{\text{module1}} = \mathbf{R}_z\left(\frac{\theta_p}{2}\right) \mathbf{T}_x(Tr_i) \mathbf{R}_z\left(\frac{\theta_p}{2}\right) \mathbf{R}_x\left(-\frac{\pi}{2}\right) \mathbf{R}_z\left(\frac{\theta_y}{2}\right) \mathbf{T}_x(Tr_{i+1}) \mathbf{R}_z\left(\frac{\theta_y}{2}\right) \mathbf{R}_x\left(\frac{\pi}{2}\right), \quad (1)$$

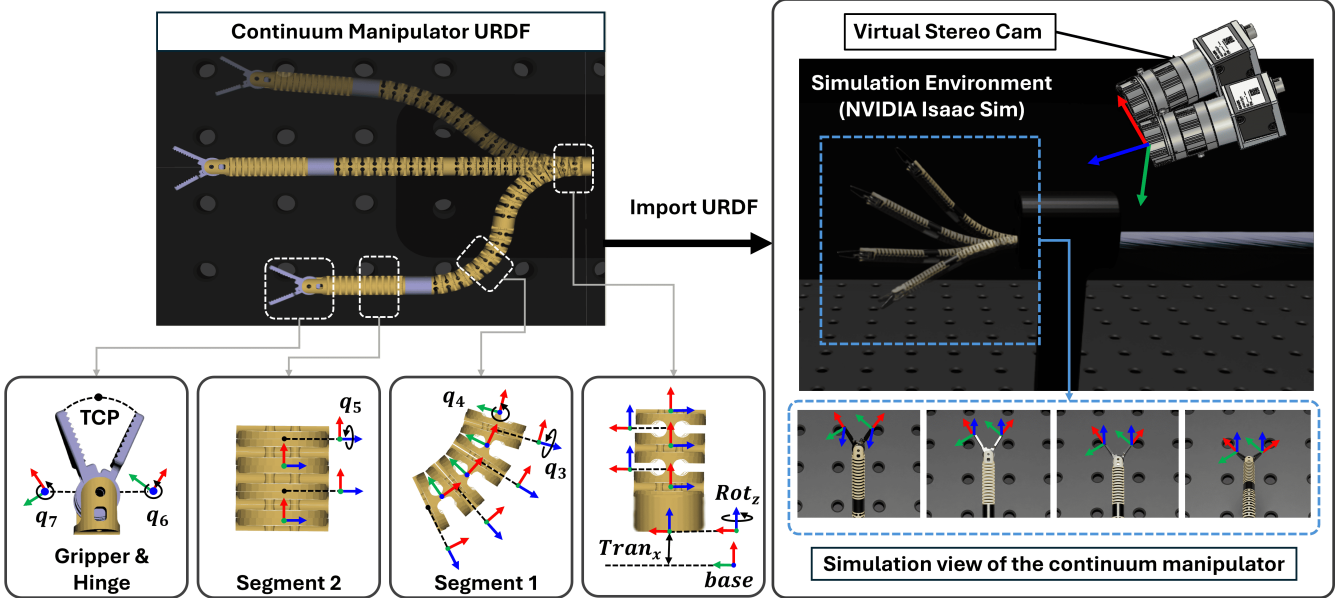


Fig. 2: URDF-based modeling and simulation pipeline for synthetic data generation. (Left) The continuum manipulator is discretized into a pseudo-rigid-body URDF comprising base rotation, bending segments, and TCP components. (Right) The model is imported into NVIDIA Isaac Sim with a calibrated stereo camera setup, enabling synchronized stereo rendering with automatic ground-truth pose annotation.

where Tr_i denotes the bending-induced translational displacement of the i -th PRB element, defined as

$$Tr_i = l \cos\left(\frac{\theta_i}{2}\right) + \frac{2h}{\theta_i} \sin\left(\frac{\theta_i}{2}\right), \quad i = 1, \dots, n, \quad (2)$$

with l and h representing the geometric parameters of the discretized segment, as illustrated in Fig. 1, which also depicts the kinematic structure of a single PRB module.

The second flexible segment undergoes single-plane bending and is modeled using the same PRB formulation, omitting the yaw-direction transformation in Equation (1).

The overall forward kinematics from the base frame to the TCP is obtained by concatenating the transformations of all PRB modules and rigid connectors:

$$\mathbf{T}_{\text{TCP}} = \mathbf{T}_{\text{trans}} \mathbf{T}_{\text{rot}} \mathbf{T}_{\text{module1}} \mathbf{T}_{\text{connector}} \mathbf{T}_{\text{module2}} \mathbf{T}_{\text{hinge}} \mathbf{T}_{\text{TCP}}. \quad (3)$$

B. Jacobian and Inverse Kinematics

The geometric Jacobian is constructed by accumulating the velocity contributions of each joint variable from the base to the TCP along the PRB chain. Within each PRB module, the rotational and bending-induced translational motions are sequentially propagated according to the transformation structure in Equation (1). The resulting Jacobian maps the joint variables $\mathbf{q} = [q_1, q_2, q_3, q_4, q_5, r]^\top$ to the TCP spatial velocity as

$$\mathbf{J} = \begin{bmatrix} \mathbf{J}_v \\ \mathbf{J}_\omega \end{bmatrix}. \quad (4)$$

where $r = (q_6 + q_7)/2$ represents the equivalent gripper yaw variable associated with the TCP definition.

Inverse kinematics is solved iteratively using a Newton-Raphson update with the Jacobian pseudoinverse:

$$\mathbf{q}_{k+1} = \mathbf{q}_k + \mathbf{J}^\dagger(\mathbf{q}_k) (\mathbf{x}_d - \mathbf{f}(\mathbf{q}_k)), \quad (5)$$

where $\mathbf{f}(\mathbf{q})$ denotes the forward kinematics and \mathbf{x}_d is the desired TCP pose.

IV. SYNTHETIC DATA GENERATION

To train the proposed stereo-based 6D pose estimation framework, we construct a physics-grounded, photo-realistic simulation pipeline for the continuum manipulator. The simulator enables large-scale automatic generation of synchronized stereo image pairs together with segmentation masks, bounding boxes, keypoints, and corresponding 6D pose annotations. This section describes the robot modeling procedure, simulation environment, automated ground-truth generation, domain randomization strategy, and dataset composition.

A. URDF Modeling of the Continuum Manipulator

The continuum manipulator provides seven degrees of freedom (DOFs), including axial translation (q_1), base rotation (q_2), two bending DOFs in the first segment (pitch q_3 and yaw q_4), one bending DOF in the second segment (pitch q_5), and independent yaw motions of the two gripper jaws (q_6, q_7).

To approximate continuous backbone deformation within a pseudo-rigid-body formulation, the manipulator is modeled using a custom URDF composed of discretized slit-type revolute joints (see Fig. 2). Each slit is implemented as a revolute joint following the kinematic formulation in Section III-A. The first bending segment is represented by 22 slit joints arranged to realize two orthogonal bending directions, enabling combined pitch and yaw motion. The second bending segment is modeled with 22 slit joints providing single-axis bending. Each slit joint is constrained to a rotation range of approximately ± 0.16 rad, such that the total bending angle of each segment is determined by

● : Key Point

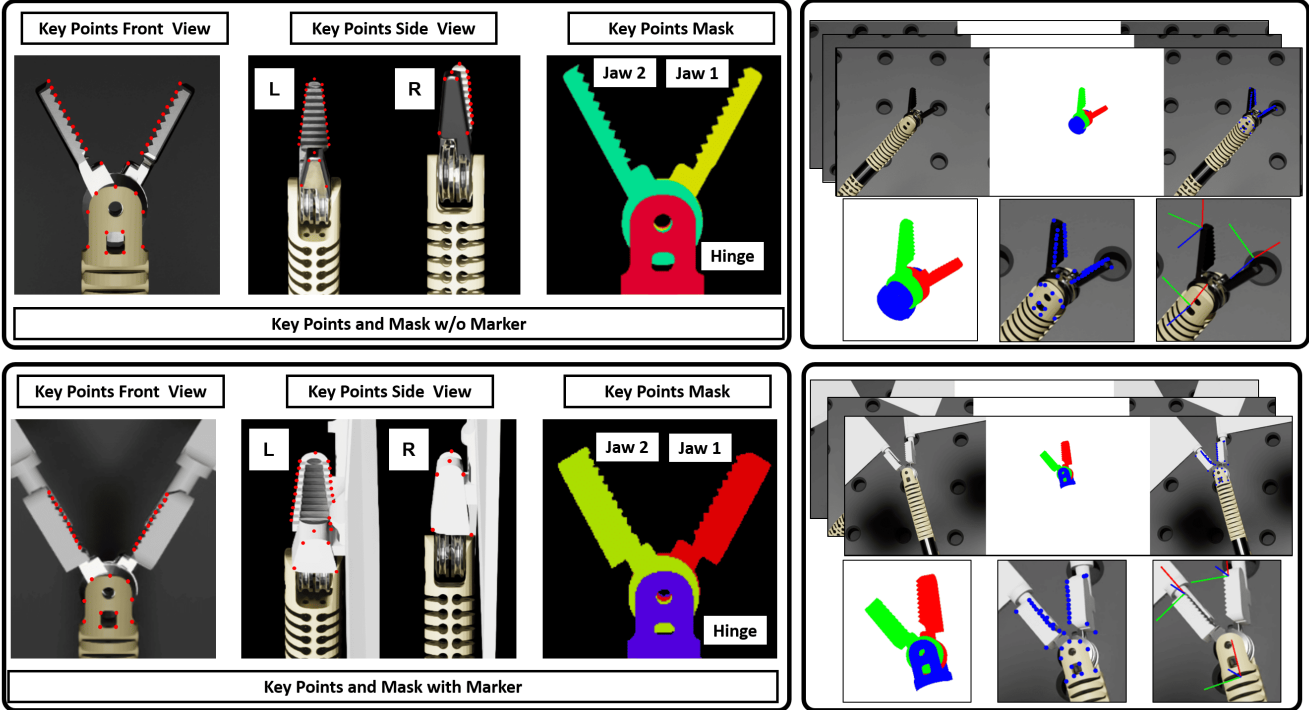


Fig. 3: Ground-truth annotation configuration. (Left, top) Keypoint and mask definitions for the marker-free configuration: 65 keypoints (28 per jaw, 9 on hinge) and four-class segmentation masks. (Left, bottom) Marker-based configuration used for real-world ground-truth acquisition. (Right) Example synthetic stereo pairs with automatically generated keypoint coordinates and 6D pose labels.

cumulative rotation across all slit joints:

$$\theta_{\text{segment}} = \sum_{k=1}^{n_{\text{slit}}} \theta_k. \quad (6)$$

In addition, a prismatic joint with a 0–30 mm stroke models axial insertion. The base rotation and gripper yaw motions are modeled as independent revolute joints, as illustrated in Fig. 2. This URDF-based representation enables integration of the continuum manipulator into NVIDIA Isaac Sim, allowing kinematically consistent articulation and geometry-aware photo-realistic rendering within the simulation environment.

B. Simulation Environment and Rendering

All data are generated in NVIDIA Isaac Sim 4.0.0, which integrates GPU-accelerated PhysX rigid-body physics simulation with path-traced photo-realistic rendering (see Fig. 2). The physics engine enforces joint limits, kinematic constraints, and collision handling, ensuring physically plausible configurations of the discretized continuum structure while preventing self-penetration among densely spaced slit joints. Although material-level continuum effects such as hysteresis are not explicitly modeled, the simulator provides constraint-consistent articulated motion suitable for large-scale geometric data generation.

Rendering is performed using physically based materials to approximate the optical properties of the continuum manipulator. The jaw surfaces are assigned a physical steel

material template with tunable metallic and surface roughness parameters, while the backbone segments are modeled using diffuse materials subject to domain randomization (Section IV-D). Illumination is configured using a combination of hemispherical environment lighting and a directional light source.

A virtual stereo RGB camera pair is configured using intrinsics calibrated from the real system (focal length 12.465 mm, resolution 2048 × 1536 px) and a baseline of 63.3 mm. Simulation runs at a 1 ms physics timestep, and frames are captured at 30 fps after the manipulator reaches static equilibrium. For each frame, synchronized stereo images, segmentation masks, and $SE(3)$ poses of Jaw 1, Jaw 2, and the hinge are recorded in the left camera frame.

C. Simulation-Driven Ground-Truth Generation

All supervision signals are generated directly within the simulation environment without any manual annotation. The proposed pipeline produces geometry-consistent keypoints, visibility labels, segmentation masks, bounding boxes, and 6D pose annotations for every rendered frame.

a) Keypoints and Visibility.: A total of 65 keypoints are defined to capture the articulated geometry: 28 keypoints along each jaw and 9 on the hinge component (Fig. 3). Each keypoint is defined in the local body frame and projected onto the image plane using the camera projection matrix.

Visibility is determined from the rendered point cloud.

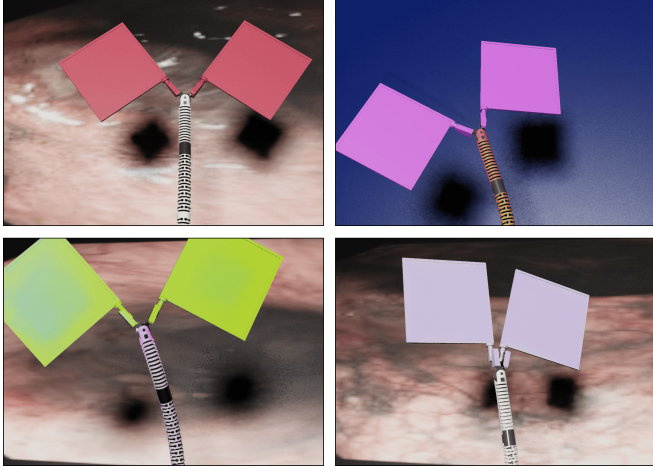


Fig. 4: Four representative examples of domain-randomized synthetic data. In each sample, background texture, backbone diffuse color, marker appearance, and jaw metallic properties are jointly randomized to maximize visual diversity across the training set.

A keypoint is labeled as visible if the Euclidean distance between its 3D position and the nearest rendered point is below 0.05 mm. Each keypoint is represented as $\{x_k, y_k, \rho_k\}$, where $\rho_k \in \{0, 1\}$ denotes visibility.

b) *Segmentation Masks and Bounding Boxes.*: Pixel-wise semantic segmentation assigns each pixel to one of four classes: background, Jaw 1, Jaw 2, or Hinge (Fig. 3). A depth-adaptive bounding box is constructed around the projected hinge center $\mathbf{c} = (u_0, v_0)$ as

$$B = [u_0 - m, v_0 - m, u_0 + m, v_0 + m], \quad m = \alpha z, \quad (7)$$

where z denotes the depth of the hinge center in the camera coordinate frame, which ranges from 200 mm to 300 mm in our dataset, and α is a fixed scaling factor.

c) *6D Pose Annotation.*: For each frame, the simulator provides the 6D poses of Jaw 1, Jaw 2, and the hinge expressed in the left camera frame, as illustrated in Fig. 2: $cam^L\mathbf{T}_{jaw1}$, $cam^L\mathbf{T}_{jaw2}$, and $cam^L\mathbf{T}_{hinge} \in SE(3)$.

The tool center point (TCP) pose used for quantitative evaluation and closed-loop control is analytically reconstructed from the dual-jaw geometry. Let $\mathbf{u}_i = \mathbf{R}_{jaw_i}\mathbf{e}_x$ denote the approach direction of each jaw, where $\mathbf{e}_x = [1, 0, 0]^\top$. The jaw opening angle is computed as

$$\theta = \cos^{-1}(\mathbf{u}_1^\top \mathbf{u}_2), \quad (8)$$

and the TCP orientation is defined by a half-angle rotation between the two jaw frames:

$$\mathbf{R}_{tcp} = \mathbf{R}_{jaw2} \mathbf{R}_z \left(\frac{\theta}{2} \right). \quad (9)$$

The TCP position is obtained as

$$\mathbf{t}_{tcp} = \frac{\mathbf{t}_{jaw1} + \mathbf{t}_{jaw2}}{2} + \mathbf{R}_{tcp} \mathbf{e}_x d \left(1 - \cos \frac{\theta}{2} \right), \quad (10)$$

where d denotes the known jaw length.

D. Domain Randomization

To improve robustness to real-world visual variability, domain randomization is applied along three axes.

a) *Backgrounds.*: Background images are sampled from a pool of 500 candidates comprising solid-color textures and endoscopic surgical scenes [35].

b) *Backbone Appearance.*: The diffuse color of backbone segments is uniformly randomized in RGB space to prevent overfitting to prototype-specific appearance.

c) *Jaw Material Properties.*: Jaw meshes retain physically based metallic shading, with metallic coefficients uniformly sampled in $[0.4, 1.0]$ to emulate surface reflectance variation.

E. Dataset Composition

For ablation studies (Section VI-A), a non-randomized subset of 30,000 stereo pairs is used, consisting of 24,000 training and 6,000 validation samples. For the full training pipeline targeting real-world deployment (Section VIII), the complete dataset of 200,000 domain-randomized stereo pairs is employed.

The dataset is defined as

$$\mathcal{D} = \{(I_i, \mathbf{S}_i, \mathbf{B}_i, \mathbf{K}_i, cam^L\mathbf{T}_{comp,i})\}_{i=1}^N, \quad (11)$$

where I_i denotes the RGB image, \mathbf{S}_i the segmentation mask, \mathbf{B}_i the bounding box, $\mathbf{K}_i \in \mathbb{R}^{J \times 2}$ ($J=65$) the 2D keypoints with corresponding visibility flags, and $cam^L\mathbf{T}_{comp,i} \in SE(3)$ the poses of Jaw 1, Jaw 2, and the hinge expressed in the left camera frame.

Joint-space sampling spans the full mechanical limits of the manipulator: axial translation $q_1 \in [0, 10]$ mm, base rotation $q_2 \in [-45^\circ, 45^\circ]$, and bending and jaw motions $q_{3-7} \in [-60^\circ, 60^\circ]$. To enforce physically valid grasp configurations, the relative jaw angles are constrained to prevent self-intersection. This sampling strategy ensures dense coverage of the reachable configuration space, including extreme bending poses and multi-segment interactions along randomized joint trajectories.

V. POSE ESTIMATION FRAMEWORK

This section presents a geometry-aware pose estimation framework integrating multi-feature fusion with rendering-based refinement. Unlike conventional direct-regression pipelines, the proposed method explicitly enforces cross-modal geometric consistency by aligning predicted structural cues with differentiably rendered observations, enabling accurate pose recovery without iterative optimization. As illustrated in Fig. 5, the architecture consists of two main stages: (i) a multi-feature fusion network (MFFN) that jointly predicts keypoints, segmentation masks, and heatmaps, and leverages the resulting geometric cues to estimate an initial 6D tool pose; and (ii) a rendering-based refinement module that predicts residual pose corrections by comparing rendered keypoints and segmentation masks from the initial pose with the visual observations produced by the MFFN in a single feed-forward pass, yielding the final refined pose without iterative optimization.

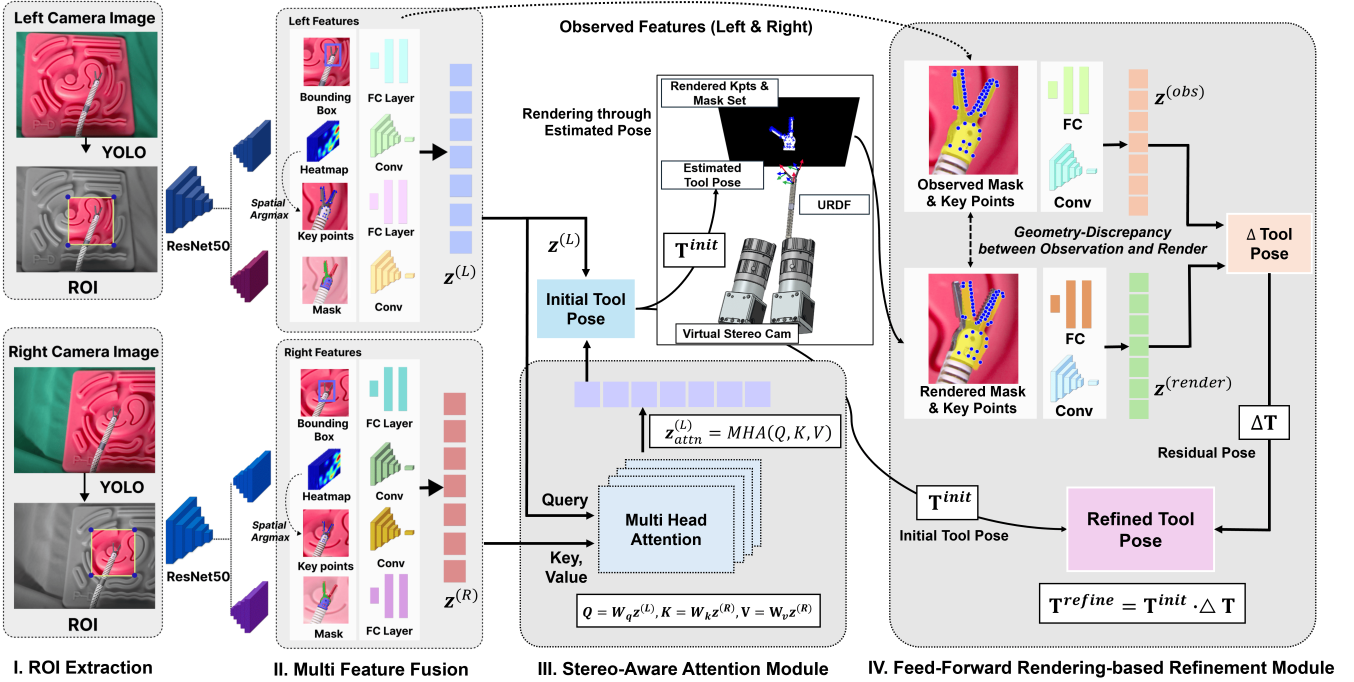


Fig. 5: Overview of the proposed stereo-aware pose estimation framework. (I) ROI Extraction: A YOLO detector localizes the manipulator in left and right stereo images. (II) Multi-Feature Fusion: A shared ResNet-50 encoder extracts keypoints, heatmaps, segmentation masks, and refined bounding boxes, which are embedded and concatenated for pose regression. (III) Stereo-Aware Attention: Cross-view features are aggregated via multi-head attention, using the left view as the query and the right view as key-value pairs. (IV) Rendering-Based Refinement: The initial pose is rendered, and geometric discrepancies between rendered and observed features are used to predict residual pose corrections in a single feed-forward pass.

A. Region-of-Interest Extraction

A YOLO-based detector localizes the manipulator and outputs a bounding box $\mathbf{B} = [x_{\min}, y_{\min}, x_{\max}, y_{\max}]$, which is used to crop the input image prior to feature extraction. This operation suppresses background clutter and improves computational efficiency. This localization step is important in minimally invasive surgery, where specular highlights, tissue deformation, and cluttered backgrounds can severely degrade feature learning if the full image is processed.

The ROI-cropped image is defined as

$$\tilde{I}(\xi, \eta) = I(x_{\min} + \xi, y_{\min} + \eta), \quad \xi \in [0, w_B], \eta \in [0, h_B], \quad (12)$$

where $w_B = x_{\max} - x_{\min}$ and $h_B = y_{\max} - y_{\min}$ denote the bounding box width and height.

B. Multi-Feature Fusion Network

The MFFN jointly estimates dense semantic segmentation, sparse geometric keypoints, heatmap distributions, and refined spatial extents. These complementary modalities capture both global part-level geometry and fine-grained structural landmarks, enabling robust pose inference under occlusion and appearance variations.

The network outputs the initial pose of jaw 1, jaw 2, and the hinge with respect to the left camera frame, together with predicted geometric features:

$$\Omega_{ref} = \{\hat{\mathbf{S}}, \hat{\mathbf{K}}\} \quad (13)$$

where $\hat{\mathbf{S}}$ denotes estimated segmentation masks, $\hat{\mathbf{K}}$ the estimated keypoint coordinates and visibility. For the monocular

configuration,

$$\Omega_{ref}^{(L)}, \text{cam}^L \hat{T}_{jaw1,2,hinge}^{(init)} = \text{MFFN}^{mono}(\tilde{I}_L), \quad (14)$$

while the stereo configuration is given by

$$\Omega_{ref}^{(L,R)}, \text{cam}^L \hat{T}_{jaw1,2,hinge}^{(init)} = \text{MFFN}^{stereo}(\tilde{I}_L, \tilde{I}_R). \quad (15)$$

C. Keypoint Detection Module

The keypoint branch predicts $K = 65$ geometric landmarks distributed along the manipulator structure. Given a shared ResNet-50 feature tensor $\mathbf{F} \in \mathbb{R}^{B \times 2048 \times u_f \times v_f}$, an upsampling decoder produces heatmaps $\mathbf{H} \in \mathbb{R}^{B \times K \times u_k \times v_k}$, with $u_f = u/8$ and $u_k = u/4$.

Continuous keypoint coordinates are obtained via differentiable Spatial SoftArgmax [36]:

$$\pi_k(i, j) = \frac{\exp(\mathbf{H}_k(i, j))}{\sum_{i', j'} \exp(\mathbf{H}_k(i', j'))}, \quad (16)$$

$$(\hat{x}_k, \hat{y}_k) = \left(\sum_{i, j} j \pi_k(i, j), \sum_{i, j} i \pi_k(i, j) \right). \quad (17)$$

Each keypoint is additionally assigned a visibility confidence $\rho_k \in [0, 1]$ predicted by a sigmoid-activated head, representing landmark reliability under occlusion.

D. Segmentation Module

The segmentation branch predicts a four-class semantic mask $\mathbf{S} \in \mathbb{R}^{B \times 4 \times H \times W}$ corresponding to background, jaw 1, jaw 2, and hinge regions. This part-aware decomposition enables the downstream pose head to disentangle rigid transformations of individual components instead of estimating a

single monolithic pose. A DeepLabv3-style ASPP decoder maps the shared feature representation \mathbf{F} to low-resolution part probability maps, which are upsampled via bilinear interpolation:

$$\hat{\mathbf{S}} = \text{Interp}(\mathcal{C}_{seg}(\mathbf{F})). \quad (18)$$

E. Pose Regression Head

The pose regression head estimates the initial 6D poses of jaw 1, jaw 2, and the hinge with respect to the left camera frame by integrating heterogeneous geometric cues. Rather than collapsing all modalities into a single shared representation at the feature level, we first encode each cue into a modality-specific latent embedding. These embeddings are then fused into a unified latent space for pose regression, preserving complementary structural information while preventing dominant appearance features from overwhelming sparse geometric signals.

Foreground segmentation refines the ROI by computing a mask-derived bounding box

$$\hat{\mathbf{B}}_{refined} = [\min_{\mathcal{M}}(\xi, \eta), \max_{\mathcal{M}}(\xi, \eta)], \quad (19)$$

where \mathcal{M} denotes the foreground pixel set of the predicted segmentation mask \mathbf{S} . The refined ROI is encoded as an additional geometric cue for pose regression.

Dense spatial outputs are embedded through convolutional projection networks that progressively compress spatial dimensions via strided convolutions:

$$\mathbf{z}_{heat} = \phi_{heat}(\mathbf{H}), \quad \mathbf{z}_{seg} = \phi_{seg}(\hat{\mathbf{S}}), \quad (20)$$

where $\phi_{heat}(\cdot)$ and $\phi_{seg}(\cdot)$ denote multi-layer convolutional encoders whose stride operations reduce the spatial resolution to a compact latent vector representation.

Sparse geometric cues are embedded through fully connected projections:

$$\mathbf{z}_{kpt} = \phi_{kpt}(\hat{\mathbf{K}}), \quad \mathbf{z}_{box} = \phi_{box}(\hat{\mathbf{B}}_{refined}), \quad (21)$$

with $\phi_{kpt}(\cdot)$ incorporating visibility-weighted keypoint coordinates. The modality embeddings are fused by concatenation:

$$\mathbf{z}_{fuse} = [\mathbf{z}_{seg}, \mathbf{z}_{heat}, \mathbf{z}_{kpt}, \mathbf{z}_{box}]. \quad (22)$$

Regression heads predict the initial pose of jaw1, jaw2, and hinge:

$$\begin{aligned} \hat{\mathbf{t}}_i^{(init)} &= g_i^{(t)}(\mathbf{z}_{fuse}), \\ \hat{\mathbf{q}}_i^{(init)} &= g_i^{(r)}(\mathbf{z}_{fuse}), \quad i \in \{\text{jaw1, jaw2, hinge}\}. \end{aligned} \quad (23)$$

where $g_i^{(t)}(\cdot)$ and $g_i^{(r)}(\cdot)$ denote component-specific fully connected regression heads for translation and rotation, respectively.

The predicted pose of each component is expressed as

$${}^{camL}\hat{T}_{i, \text{jaw1,2,hinge}}^{(init)} = [\hat{\mathbf{t}}_i, \hat{\mathbf{q}}_i], \quad (24)$$

with $\hat{\mathbf{t}}_i \in \mathbb{R}^3$ and $\hat{\mathbf{q}}_i \in \mathbb{S}^3$ representing translation and unit quaternion orientation.

F. Stereo-Aware Attention Module

For stereo configurations, geometric features extracted from the left and right camera views are fused using a multi-head attention mechanism to exploit cross-view geometric consistency. This mechanism allows the model to learn epipolar-consistent correspondences implicitly, avoiding explicit triangulation while still exploiting stereo constraints. Let $\mathbf{z}^{(L)}$ and $\mathbf{z}^{(R)}$ denote the fused latent embeddings obtained from the left and right views, respectively, as described in Section V-E.

Cross-view feature aggregation is performed by treating the left-view embedding as the query and the right-view embedding as key-value pairs:

$$\begin{aligned} \mathbf{Q} &= W_q \mathbf{z}^{(L)}, & \mathbf{K} &= W_k \mathbf{z}^{(R)}, & \mathbf{V} &= W_v \mathbf{z}^{(R)}, \\ \mathbf{z}_{attn}^{(L)} &= \text{MultiHead}(\mathbf{Q}, \mathbf{K}, \mathbf{V}) \end{aligned} \quad (25)$$

where W_q , W_k , and W_v are learned linear projections and the attention module employs four heads. The stereo-enhanced latent representation is then constructed as

$$\mathbf{z}_{stereo} = [\mathbf{z}^{(L)}, \mathbf{z}_{attn}^{(L)}], \quad (26)$$

which integrates monocular geometric cues with cross-view contextual information. For stereo pose estimation, \mathbf{z}_{stereo} replaces \mathbf{z}_{fuse} as the input to the pose regression on (23).

G. Feed-Forward Rendering-Based Refinement Module

Although feed-forward pose regression enables efficient inference, the predicted poses may remain inconsistent with the observed image evidence due to residual perception errors. To address this limitation, we introduce a learned pose-consistency module that compares predicted visual cues against differentiable renderings of the CAD model. In contrast to prior render-and-compare approaches that rely on iterative optimization [15], our module performs feed-forward rendering-based refinement in a single pass, substantially reducing inference time while preserving geometric consistency.

Given the initial pose estimates ${}^{camL}\hat{T}_i^{(init)}$, $i \in \{\text{jaw1, jaw2, hinge}\}$, a differentiable renderer synthesizes geometric observations from known CAD mesh models:

$$\Omega_{init}^{(L,R)} = \text{Renderer}\left({}^{camL}\hat{T}_i^{(init)}, \mathcal{M}, {}^{cam(L,R)}T_{base}\right), \quad (27)$$

where \mathcal{M} denotes the articulated link meshes and ${}^{cam(L,R)}T_{base}$ represent the calibrated camera-to-base extrinsic transformations. For the right camera, the predicted left-frame pose is transformed using known stereo extrinsics to ensure consistent cross-view rendering.

Both rendered geometric outputs and estimated keypoints and mask from the MFFN ($\Omega_{ref}^{(L,R)}$) are embedded into latent representations using modality-specific encoders described in Section V-E:

$$\mathbf{z}_{init} = \Phi_{init}(\Omega_{rend}^{(L,R)}), \quad \mathbf{z}_{obs} = \Phi_{obs}(\Omega_{ref}^{(L,R)}). \quad (28)$$

A refinement network then estimates the residual pose correction by comparing rendered and observed embeddings:

$$[\Delta\hat{\mathbf{t}}_i, \Delta\hat{\mathbf{q}}_i] = r_\phi(\mathbf{z}_{obs}, \mathbf{z}_{init}), \quad (29)$$

where $r_\phi(\cdot)$ denotes a lightweight feed-forward correction network.

The refined pose is obtained by residual composition:

$$\hat{\mathbf{t}}_i^{(refine)} = \hat{\mathbf{t}}_i^{(init)} + \Delta\hat{\mathbf{t}}_i, \quad (30)$$

$$\hat{\mathbf{q}}_i^{(refine)} = \hat{\mathbf{q}}_i^{(init)} \otimes \Delta\hat{\mathbf{q}}_i, \quad (31)$$

with \otimes denoting quaternion multiplication. The refined transformation of each component is expressed as

$$camL\hat{T}_i^{(refine)} = [\hat{\mathbf{t}}_i^{(refine)}, \hat{\mathbf{q}}_i^{(refine)}]. \quad (32)$$

Unlike iterative optimization-based refinement methods, the proposed module performs pose correction in a single forward pass, enabling real-time inference while maintaining rendering consistency with observed geometric cues.

H. Loss Formulation and Multi-Stage Training

The proposed framework is optimized using stage-specific objectives aligned with the learning purpose of each module. This multi-stage training strategy stabilizes convergence and mitigates gradient interference between visual perception and 6D pose estimation. Both monocular and stereo configurations follow the same training pipeline, with the only difference being the inclusion of the stereo-aware attention module in the stereo setting.

Stage 1: Visual Perception Learning: In the first stage, the YOLO-based detector is trained independently for region localization using standard detection losses. The segmentation, keypoint, and visibility branches are jointly optimized using a composite perception objective:

$$\mathcal{L}_{\text{perc}} = \lambda_{\text{seg}}\mathcal{L}_{\text{seg}} + \lambda_{\text{kpt}}\mathcal{L}_{\text{kpt}} + \lambda_{\text{vis}}\mathcal{L}_{\text{vis}}. \quad (33)$$

The segmentation loss enforces both pixel-wise classification accuracy and region-level overlap:

$$\mathcal{L}_{\text{seg}} = \text{BCE}(\hat{\mathbf{S}}, \mathbf{S}) + \left(1 - \frac{2\langle \hat{\mathbf{S}}, \mathbf{S} \rangle}{\|\hat{\mathbf{S}}\|_1 + \|\mathbf{S}\|_1}\right), \quad (34)$$

where the ground-truth segmentation mask \mathbf{S} is one-hot encoded across four semantic classes (background, jaw 1, jaw 2, and hinge).

Keypoint localization is supervised using a visibility-weighted Smooth ℓ_1 loss:

$$\mathcal{L}_{\text{kpt}} = \frac{1}{K} \sum_{j=1}^K \rho_j \text{SmoothL1}(\hat{\mathbf{k}}_j - \mathbf{k}_j), \quad (35)$$

where $\rho_j \in [0, 1]$ denotes the predicted visibility of the j -th keypoint. The Smooth ℓ_1 function is defined as

$$\text{SmoothL1}(x) = \begin{cases} \frac{x^2}{2\beta}, & |x| < \beta, \\ |x| - \frac{\beta}{2}, & \text{otherwise,} \end{cases} \quad \beta = 0.01. \quad (36)$$

Visibility estimation is optimized using binary cross-entropy:

$$\mathcal{L}_{\text{vis}} = \text{BCE}(\hat{\boldsymbol{\rho}}, \boldsymbol{\rho}). \quad (37)$$

Stage 2: Pose Regression Training: After learning stable visual representations, all perception branches are frozen. The pose regression head is then trained to estimate the initial 6D poses of jaw 1, jaw 2, and the hinge, each consisting of a translation and a rotation.

The pose supervision is formulated as a weighted combination of translation and orientation errors:

$$\mathcal{L}_{\text{pose}} = \sum_i \lambda_t \|\hat{\mathbf{t}}_i^{(init)} - \mathbf{t}_i\|_2^2 + \lambda_r (1 - \langle \hat{\mathbf{q}}_i^{(init)}, \mathbf{q}_i \rangle) \quad (38)$$

where $\hat{\mathbf{t}}_i^{(init)} \in \mathbb{R}^3$ and $\hat{\mathbf{q}}_i^{(init)} \in \mathbb{S}^3$ denote the predicted initial translation and unit quaternion rotation of component $i \in \{\text{jaw1, 2, hinge}\}$, respectively, and $(\mathbf{t}_i, \mathbf{q}_i)$ represent the corresponding ground-truth pose.

The translation term is supervised using mean squared error, while the rotation term employs a cosine similarity loss on unit quaternions.

Stage 3: Rendering-Based Refinement: Finally, the refinement module is trained to predict residual pose corrections while freezing all preceding components. Rather than directly regressing the refined pose, the network learns the residual transformation that maps the initial prediction to the ground-truth pose.

Given the initial pose estimates $(\hat{\mathbf{t}}_i^{(init)}, \hat{\mathbf{q}}_i^{(init)})$ and the corresponding ground-truth pose $(\mathbf{t}_i, \mathbf{q}_i)$, the residual supervision is constructed as

$$\begin{aligned} \Delta\mathbf{t}_i^* &= \mathbf{t}_i - \hat{\mathbf{t}}_i^{(init)}, \\ \Delta\mathbf{q}_i^* &= (\hat{\mathbf{q}}_i^{(init)})^{-1} \otimes \mathbf{q}_i, \end{aligned} \quad (39)$$

where $(\cdot)^{-1}$ denotes quaternion conjugation.

The refinement network predicts residual corrections $(\Delta\hat{\mathbf{t}}_i, \Delta\hat{\mathbf{q}}_i)$, which are supervised using the residual pose loss:

$$\mathcal{L}_{\text{ref}} = \sum_i \lambda_t^{(\text{ref})} \|\Delta\hat{\mathbf{t}}_i - \Delta\mathbf{t}_i^*\|_2^2 + \lambda_r^{(\text{ref})} (1 - \langle \Delta\hat{\mathbf{q}}_i, \Delta\mathbf{q}_i^* \rangle). \quad (40)$$

VI. MODEL COMPONENT ABLATIONS

This section presents ablation studies conducted on a large-scale synthetic dataset generated using NVIDIA Isaac Sim, as described in Section IV-B. Each sample comprises stereo image pairs, segmentation masks, keypoints, bounding boxes, heatmaps, and the corresponding 6D poses of jaw 1, jaw 2, and the hinge expressed in the left camera frame. The dataset contains a total of 30,000 stereo pairs, with 24,000 samples used for training and 6,000 for validation. The ablation studies analyze the individual contributions of the proposed refinement module and the stereo-aware multi-feature fusion network.

A. Comparative Performance on Synthetic Data

Table I summarizes overall TCP pose estimation accuracy. Translation error is computed as the Euclidean distance between predicted and ground-truth TCP positions, while rotation error is obtained from the relative quaternion $q_{\text{rel}} = q_{\text{gt}}^{-1} \otimes q_{\text{pred}}$, whose axis-angle magnitude represents the rotational deviation.

TABLE I: Quantitative comparison of TCP pose estimation performance under monocular and stereo configurations with and without the refinement module on the synthetic dataset. Translation error is measured as Euclidean distance in millimeters, and rotation error is computed from the relative quaternion in degrees.

Method	Config	TCP Trans Err [mm]	TCP Rot Err [deg]
MFFN	Mono	0.95 ± 1.70	1.58 ± 2.19
MFFN + Refine	Mono	0.57 ± 0.90	1.40 ± 1.93
MFFN	Stereo	0.64 ± 0.35	0.95 ± 0.43
MFFN + Refine	Stereo	0.14 ± 0.10	0.44 ± 0.24

TABLE II: Axis-wise TCP pose estimation errors in the camera frame on the synthetic dataset. Translation errors are reported along the x , y , and z axes in millimeters, and orientation errors denote angular deviations between predicted and ground-truth TCP axes in degrees.

Method	Config	TCP Translation Error [mm]			TCP Axis Error [deg]		
		X	Y	Z	$cam\hat{x}_{tcp}$	$cam\hat{y}_{tcp}$	$cam\hat{z}_{tcp}$
MFFN	Mono	0.38 ± 1.2	0.28 ± 0.6	0.71 ± 1.2	1.25 ± 1.9	1.10 ± 1.5	1.34 ± 1.9
MFFN + Refine	Mono	0.10 ± 0.2	0.21 ± 0.1	0.54 ± 0.9	1.10 ± 1.6	1.00 ± 1.3	1.21 ± 1.7
MFFN	Stereo	0.29 ± 0.2	0.21 ± 0.1	0.43 ± 0.3	0.80 ± 0.4	0.70 ± 0.4	0.74 ± 0.4
MFFN + Refine	Stereo	0.05 ± 0.1	0.04 ± 0.1	0.12 ± 0.1	0.34 ± 0.2	0.34 ± 0.2	0.36 ± 0.2

The monocular MFFN achieves a translation error of 0.95 mm and a rotation error of 1.58° . Incorporating the refinement module reduces these errors to 0.57 mm and 1.40° , respectively.

Under stereo observation, the MFFN improves to 0.64 mm translation error and 0.95° rotation error, while the full MFFN + Refine framework achieves the best performance of 0.14 mm and 0.44° . This corresponds to over 78% reduction in translation error and 72% reduction on rotation error relative to the monocular MFFN model, demonstrating the complementary benefits of stereo geometry and residual pose refinement.

Table II reports axis-wise translation and orientation errors in the camera frame. Translation errors correspond to deviations along the TCP x , y , and z directions, while orientation errors quantify angular differences between predicted and ground-truth TCP axes expressed in the camera frame. Across configurations, translation errors along the z -axis are consistently larger than those along x and y , indicating increased difficulty in depth estimation. Orientation errors exhibit similar trends across the three TCP axes.

B. Effect of the Refinement Module

The refinement module enhances pose estimation by predicting residual corrections based on geometric discrepancies between the MFFN-predicted keypoints and silhouettes and their rendered counterparts generated from the initial pose estimates, as illustrated in Fig. 6.

As shown in Fig. 6, the rendered observations obtained from the refined pose, denoted as Ω_{refine} , exhibit improved alignment with the MFFN-estimated visual features Ω_{ref} compared to the rendered results from the initial pose Ω_{init} . This demonstrates that the feed-forward rendering-based refinement module effectively reduces residual pose errors and produces geometrically consistent pose estimates with respect to the observed visual features.

Quantitatively, refinement reduces translation error by approximately 40% in the monocular configuration (from

0.95 mm to 0.57 mm) and by 78% in the stereo configuration (from 0.64 mm to 0.14 mm). Improvements are consistently observed across all translational axes, indicating that residual correction operates globally rather than targeting specific directions.

Rotational accuracy also improves with refinement. In the monocular setting, rotation error decreases by about 11% (from 1.58° to 1.40°), while in the stereo configuration it is reduced by approximately 54% (from 0.95° to 0.44°). Axis-wise analysis further confirms consistent orientation improvement across all TCP axes.

C. Effect of the Stereo Configuration

Stereo observation substantially enhances pose estimation robustness by providing multiple viewpoints and explicit depth cues. Transitioning from monocular to stereo input improves the MFFN model by approximately 33% in translation accuracy (from 0.95 mm to 0.64 mm) and 40% in rotational accuracy (from 1.58° to 0.95°).

When combined with the refinement module, translation accuracy further improves by approximately 75%, decreasing from 0.57 mm to 0.14 mm, while rotational accuracy improves by about 69%, from 1.40° to 0.44° .

The most substantial improvement occurs along the camera depth direction, as shown in Table II. The z -axis translation error decreases from 0.71 mm to 0.43 mm for the MFFN model and from 0.54 mm to 0.12 mm for the MFFN + Refine framework, confirming that binocular triangulation significantly strengthens depth observability.

Furthermore, orientation errors along the TCP axes decrease more prominently under stereo observation, particularly for \hat{z}_{tcp} . For the MFFN model, the \hat{z}_{tcp} error decreases from 1.34° to 0.74° , and for the MFFN + Refine framework from 1.21° to 0.36° , indicating improved roll-pitch estimation enabled by accurate depth reconstruction.

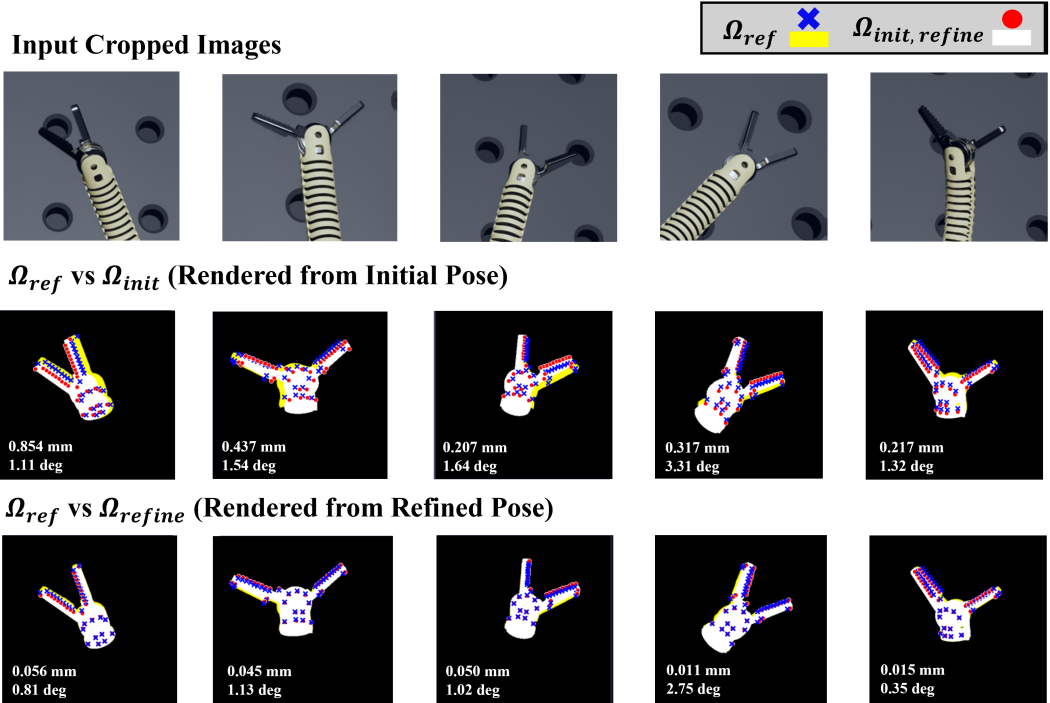


Fig. 6: Visualization of rendering-based refinement. Ω_{ref} represents the predicted keypoints (blue) and mask (yellow). $\Omega_{init, refine}$ represents the rendered keypoints (red) and mask (white), obtained from the initial pose (second row) and refined pose (third row), respectively. Refinement reduces the geometric discrepancy between Ω_{ref} and $\Omega_{init, refine}$, leading to improved translation (mm) and rotation (deg) accuracy.

TABLE III: Time efficiency and model size of each pipeline component.

Module	# Params	Inf. Time [ms]
YOLO	56.9M	16.8 ± 0.4
MFFN	84.7M	126.2 ± 13.3
Rendering (L+R)	–	59.2 ± 20.0
Refinement Module	0.84M	7.8 ± 2.9
Total	142.4M	210.0 ± 32.5

D. Time Efficiency and Model Complexity

Table III summarizes the computational cost and model size of each pipeline component. The overall framework contains 142.4 million parameters and achieves an average inference time of 210.0 ms per stereo frame pair, corresponding to approximately 4.8 Hz pose estimation frequency.

The majority of computation is dominated by the MFFN, which accounts for 126.2 ms per inference, while the rendering process for both camera views requires 59.2 ms. Notably, the proposed refinement module introduces minimal overhead, adding only 7.8 ms despite enabling substantial accuracy improvement through geometric residual correction.

Unlike conventional optimization-based pose refinement approaches that rely on iterative rendering and gradient-based updates, the proposed framework performs refinement in a single feed-forward pass. This design eliminates costly iterative loops and enables stable inference latency suitable for closed-loop robotic control.

Furthermore, the modular structure allows straightforward acceleration using optimized inference engines such as

TensorRT. With model compression and hardware-specific optimization, the proposed pipeline has strong potential to achieve real-time performance for vision-based continuum manipulator control.

VII. SIM-TO-REAL TRANSFER VIA CALIBRATION AND SELF-SUPERVISED ADAPTATION

This section presents the sim-to-real strategies employed to deploy the trained model in real surgical environments, including camera intrinsic and extrinsic calibration, domain randomization in simulation, and self-supervised real adaptation.

A. Real Camera Intrinsic and Extrinsic Calibration

To enable deployment of the simulation-trained model in real-world settings, accurate camera intrinsic and extrinsic calibration is required. Camera intrinsics are obtained using standard checkerboard-based calibration to estimate focal lengths and principal points for each camera.

Extrinsic calibration is performed following the procedure illustrated in Fig. 7. For conventional rigid robots, precise forward kinematics obtained from joint encoders enable standard hand-eye calibration. In contrast, continuum manipulators lack reliable base-to-end-effector transformations due to the absence of joint-level sensing and transmission-induced hysteresis and compliance. Consequently, classical hand-eye formulations based on forward kinematics are not directly applicable.

To address this limitation, we employ an RGB-D sensing camera to directly estimate the pose of the manip-

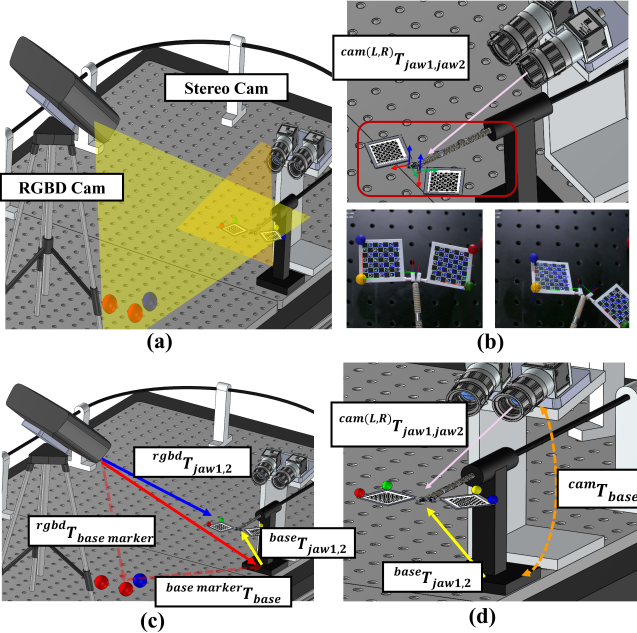


Fig. 7: Overview of the hand-eye calibration pipeline for estimating the camera-to-robot base extrinsic transformation. (a) Overall calibration workflow. (b) Stereo camera estimation of the camera-to-end-effector pose using Charuco fiducial markers. (c) RGB-D-based point cloud acquisition of base and end-effector fiducials, where center points are extracted via RANSAC to recover the robot-base-to-end-effector transformation. (d) Joint optimization of the transformations in (b) and (c) to obtain the final camera-to-robot base extrinsic parameters for simulation and real-world alignment.

ulator end-effector relative to the robot base, while a stereo camera system independently estimates the camera-to-end-effector transformation using ChArUco fiducial markers attached to the jaw case. The RGB-D camera detects three base fiducial markers and four jaw markers (two per jaw) through HSV-based segmentation and point-cloud fitting via RANSAC [37], yielding the transformations $base\mathbf{T}_{jaw1,jaw2}$. The stereo system simultaneously estimates $cam(L,R)\mathbf{T}_{jaw1,jaw2}$.

For each robot configuration i , the end-effector pose in the camera frame is obtained as

$$cam\mathbf{T}_{jaw}^{(i)}. \quad (41)$$

The robot base pose in the camera frame, $cam\mathbf{T}_{base}$, is estimated once through a static calibration procedure. The corresponding base-to-end-effector transformation is computed as

$$base\mathbf{T}_{jaw}^{(i)} = (cam\mathbf{T}_{base})^{-1} cam\mathbf{T}_{jaw}^{(i)}. \quad (42)$$

An extrinsic candidate for each configuration is then constructed as

$$cam\mathbf{T}_{base}^{(i)} = cam\mathbf{T}_{jaw}^{(i)} \left(base\mathbf{T}_{jaw}^{(i)} \right)^{-1}, \quad (43)$$

yielding a set of extrinsic estimates $\{cam\mathbf{T}_{base}^{(i)}\}_{i=1}^N$, where $N = 400$ in our experiments.

Across all configurations, the extrinsic candidates exhibit standard deviations of approximately 7–8 mm in translation

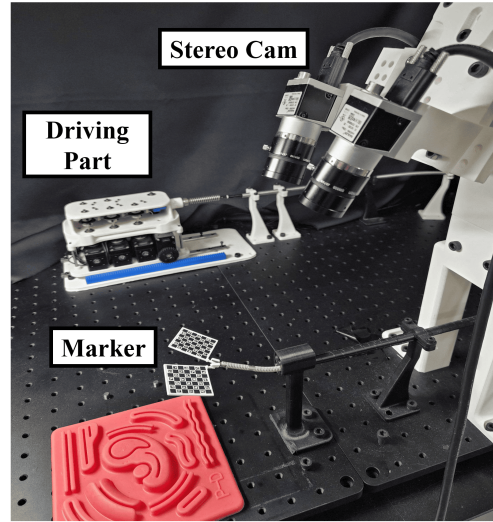


Fig. 8: Real-world experimental setup for validation. The system consists of the actuation unit, a two-segment continuum manipulator, a stereo camera pair, and jaw-mounted cases with Charuco markers for camera-to-TCP pose estimation. The manipulator is driven through approximately 1.5 m tendon-sheath transmission from the actuation unit.

and 1.4–1.5° in rotation, reflecting sensing noise, marker localization uncertainty, and configuration-dependent deformation. To obtain a robust extrinsic solution, we first compute an initial estimate by averaging translations in Euclidean space and rotations via quaternion averaging.

The extrinsic parameters are then refined by solving the following robust optimization problem:

$$\min_{\mathbf{X} \in SE(3)} \sum_i \rho \left(\left\| \mathbf{W} \log \left(\mathbf{X}^{-1} cam\mathbf{T}_{base}^{(i)} \right) \right\|^2 \right), \quad (44)$$

where $\log(\cdot)$ denotes the Lie algebra mapping from $SE(3)$ to $\mathfrak{se}(3)$, \mathbf{W} balances rotational and translational components, and $\rho(\cdot)$ is the Huber loss.

B. Self-Supervised Real Adaptation with Pseudo Ground Truth

Although camera extrinsic parameters are estimated through the calibration procedure described in Section VII-A and transferred to the simulation environment, residual errors inevitably remain due to sensor noise and calibration variance. When deploying the simulation-trained model in real-world scenarios, these extrinsic deviations alter the geometric relationship between image-space visual features (segmentation masks, keypoints, bounding boxes, and heatmaps) and the corresponding 6D poses. As a result, the pose inferred from real visual observations exhibits a consistent bias relative to the true robot configuration.

To compensate for this structured offset without requiring manual annotation, we propose a self-supervised real adaptation framework that constructs pseudo ground-truth (GT) pose supervision directly from real observations through differentiable rendering, as summarized in Algorithm 1. During deployment, the multi-feature fusion network outputs

Algorithm 1 Self-Supervised Real Adaptation with Pseudo Ground Truth Refinement

Require: Stereo images I_L, I_R , link meshes \mathcal{M} , extrinsics ${}^{cam}T_{base}^L, {}^{cam}T_{base}^R$, multi-feature fusion network f_θ , refinement module r_ϕ

Ensure: Adapted multi-feature fusion network f_{θ^*} and refinement module r_{ϕ^*}

- 1: Initialize pseudo GT buffer $\mathcal{D}_{pseudo} \leftarrow \emptyset$
- 2: // Forward prediction from stereo observation
- 3: $(\Omega_{ref}^{L,R}, \hat{T}) \leftarrow f_\theta(I_L, I_R)$
- 4: $\hat{T} \equiv {}^{cam}T_{jaw1,2,hinge}^L$
- 5: // Pseudo GT pose refinement via differentiable rendering
- 6: **for** $i = 1$ to N_{opt} **do**
- 7: $\Omega_i^{L,R} \leftarrow \text{Render}(\hat{T}, \mathcal{M}, {}^{cam}T_{base}^{L,R})$
- 8: $L_i \leftarrow \mathcal{L}_{align}(\Omega_i^{L,R}, \Omega_{ref}^{L,R})$
- 9: $\hat{T} \leftarrow \hat{T} - \alpha \nabla_{\hat{T}} L_i$
- 10: **end for**
- 11: // Store refined pseudo GT sample
- 12: $\mathcal{D}_{pseudo} \leftarrow \mathcal{D}_{pseudo} \cup \{(I_L, I_R, \hat{T})\}$
- 13: Freeze all visual perception branches of f_θ
- 14: // Few-shot real adaptation (pose regression only)
- 15: **if** $|\mathcal{D}_{pseudo}| \geq N_{pseudo}$ **then**
- 16: **for** $e = 1$ to E_{fs} **do**
- 17: Update pose regression head of f_θ and refinement module r_ϕ using \mathcal{D}_{pseudo}
- 18: **end for**
- 19: **end if**
- 20: Set $f_{\theta^*} \leftarrow f_\theta, r_{\phi^*} \leftarrow r_\phi$
- 21: **return** f_{θ^*}, r_{ϕ^*}

the estimated geometric features and initial pose:

$$\Omega_{ref}^{(L,R)}, {}^{cam}T_{jaw1,2,hinge}^{(init)} = f_\theta(I_L, I_R), \quad (45)$$

where $\Omega_{ref}^{(L,R)} = \{\hat{\mathbf{S}}^{(L,R)}, \hat{\mathbf{K}}^{(L,R)}\}$ denotes the predicted segmentation masks and keypoints with visibility.

Given the estimated pose \hat{T} and known link meshes \mathcal{M} , rendered geometric observations are generated for both camera views:

$$\Omega_{rend}^{(L,R)} = \text{Render}(\hat{T}, \mathcal{M}, {}^{cam}T_{base}^{L,R}), \quad (46)$$

where $\Omega_{rend}^{(L,R)} = \{\mathbf{S}_{rend}^{(L,R)}, \mathbf{K}_{rend}^{(L,R)}\}$ denote the rendered silhouettes and keypoints.

a) *Rendering-Based Alignment Loss:* To refine the estimated pose and construct pseudo GT supervision, we minimize a rendering-based alignment loss between the rendered and observed geometric features following a similar formulation to recent works [29]:

$$\mathcal{L}_{align} = \lambda_1 \mathcal{L}_{MSE} + \lambda_2 \mathcal{L}_{dist} + \lambda_3 \mathcal{L}_{scale} + \lambda_4 \mathcal{L}_{kpt}. \quad (47)$$

The pixel-wise silhouette consistency is enforced through a mean squared error:

$$\mathcal{L}_{MSE} = \sum_{i=0}^{H-1} \sum_{j=0}^{W-1} \left(\mathbf{S}_{rend}(i, j) - \hat{\mathbf{S}}_{ref}(i, j) \right)^2. \quad (48)$$

Since the MSE loss provides limited gradients when silhouettes do not overlap, a distance-field-based alignment term is introduced. A distance field is constructed from the reference silhouette:

$$\mathbf{D}_{ref}(i, j) = \begin{cases} 0, & \hat{\mathbf{S}}_{ref}(i, j) = 1, \\ \frac{\text{dist}(i, j)}{\gamma}, & \hat{\mathbf{S}}_{ref}(i, j) = 0, \end{cases} \quad (49)$$

where $\text{dist}(i, j)$ denotes the Euclidean distance to the nearest foreground pixel and γ is a decay factor. The corresponding loss is defined as

$$\mathcal{L}_{dist} = \sum_{i=0}^{H-1} \sum_{j=0}^{W-1} \mathbf{S}_{rend}(i, j) \mathbf{D}_{ref}(i, j). \quad (50)$$

To regulate scale consistency between the rendered model and observed silhouettes, both masks are normalized by their foreground pixel counts, and the scale loss is computed as

$$\mathcal{L}_{scale} = \left| \frac{\sum_{i,j} \mathbf{S}_{rend}(i, j)}{\sum_{i,j} \mathbf{S}_{ref}(i, j)} - \frac{\sum_{i,j} \hat{\mathbf{S}}_{ref}(i, j)}{\sum_{i,j} \hat{\mathbf{S}}_{ref}(i, j)} \right|. \quad (51)$$

Keypoint alignment is enforced only on visible landmarks using a visibility-weighted Smooth ℓ_1 loss:

$$\mathcal{L}_{kpt} = \frac{1}{K} \sum_{j=1}^K \rho_j \text{SmoothL1}(\mathbf{K}_{rend}^j - \hat{\mathbf{K}}_{ref}^j), \quad (52)$$

where $\rho_j \in [0, 1]$ is the predicted visibility confidence of the j -th keypoint.

b) *Pseudo Ground Truth Refinement and Adaptation:* Starting from the initial pose $\hat{T}^{(init)}$, iterative gradient descent on \mathcal{L}_{align} yields a refined pose \hat{T}^* that geometrically aligns the rendered observations with real visual features. This refined pose is treated as pseudo ground truth and accumulated in the buffer \mathcal{D}_{pseudo} .

Examples of the resulting pseudo GT poses obtained from multiple real stereo image pairs are illustrated in Fig. 9, demonstrating consistent convergence from biased initial estimates toward geometrically aligned solutions using the MFFN-predicted segmentation masks and keypoints.

Once sufficient pseudo GT samples (150 real images in our implementation) are collected, both the pose regression head of the MFFN and the feed-forward rendering-based refinement module are fine-tuned using \mathcal{D}_{pseudo} , while all visual perception branches (segmentation, keypoint detection, and attention modules) remain frozen. This selective adaptation corrects extrinsic-induced pose bias while preserving robust visual feature extraction learned from large-scale synthetic data.

This self-supervised adaptation process enables accurate real-world deployment without manual annotation and substantially improves sim-to-real generalization for continuum manipulator pose estimation.

C. Effect of Jaw Case Attachment on Pose Estimation Accuracy

Accurate ground-truth pose acquisition in a fully markerless real-world setting is inherently challenging. To enable

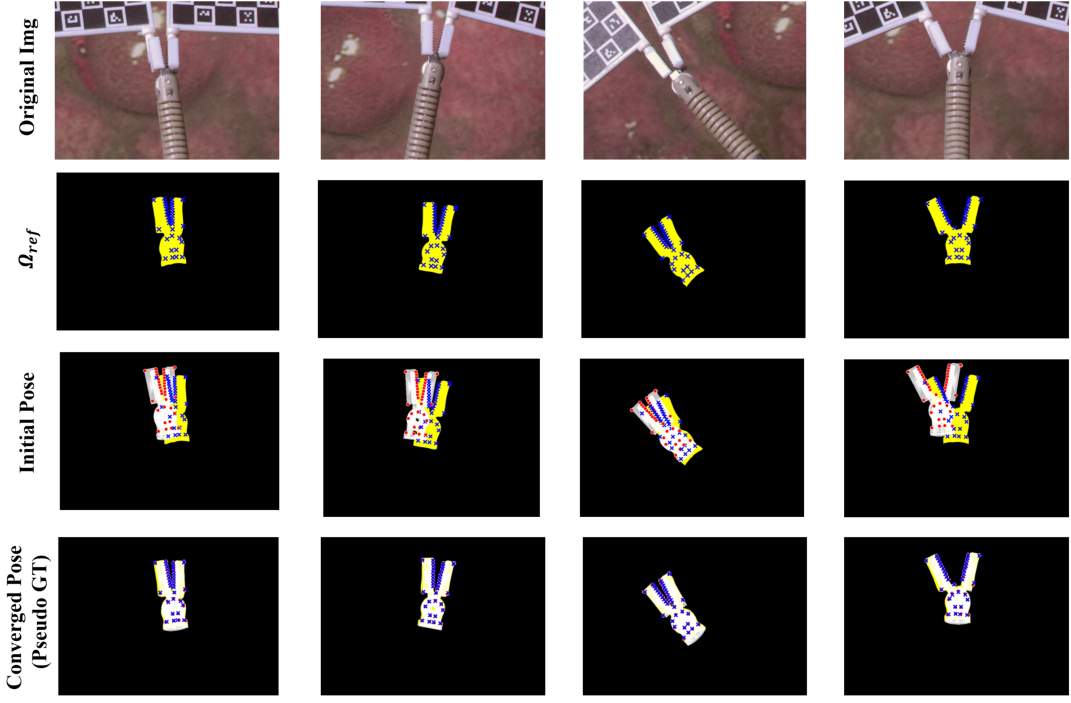


Fig. 9: Rendering-based pseudo ground-truth generation for self-supervised real adaptation. From a real input image (top row), the network predicts keypoints and masks (Ω_{ref}). An initial pose is estimated and rendered based on these predictions (third row), and geometric discrepancy between predicted and rendered features is iteratively minimized. The converged pose (bottom row) is treated as pseudo ground truth, enabling self-supervised adaptation without external tracking systems.

reliable quantitative evaluation, a detachable jaw case is employed during validation, on which a ChArUco marker is attached solely for ground-truth measurement (see Fig. 8). Importantly, the proposed model explicitly excludes the marker region from segmentation masks and keypoint definitions, ensuring that pose estimation remains independent of marker appearance, as illustrated in Fig. 3.

Table IV compares pose estimation accuracy with and without the jaw case geometry. Although the jaw case facilitates precise ground-truth acquisition, the proposed framework itself operates in a fully markerless manner during inference.

The performance difference between the jaw-case-attached and non-attached configurations is negligible: translation error increases marginally from 0.14 mm to 0.17 mm, and rotation error from 0.44° to 0.53° . These results indicate that the additional structure does not introduce artificial bias or unintended cues into the pose estimation pipeline.

Overall, the proposed method demonstrates robustness to minor geometric variations, and the jaw case serves exclusively as a ground-truth acquisition tool without affecting pose estimation performance.

VIII. MODEL VALIDATION IN REAL ENVIRONMENTS

For real-world validation, ground-truth poses of jaw 1 and jaw 2 are obtained using Charuco markers attached to each jaw. Four different endoscopic surgical backgrounds from [35] are utilized to introduce visual diversity. For each background, random motion trajectories containing 250

TABLE IV: Effect of jaw case attachment on TCP pose estimation accuracy in the synthetic dataset. Results compare models trained with and without the jaw case geometry to assess its impact on performance.

Method	Jaw Case	TCP Trans Err [mm]	TCP Rot Err [deg]
MFFN + Refine (Stereo)	Off	0.14 ± 0.10	0.44 ± 0.24
MFFN + Refine (Stereo)	On	0.17 ± 0.12	0.53 ± 0.30

distinct joint configurations are collected, resulting in a total of 1,000 real validation samples.

We evaluate four network variants: stereo-aware MFFN, stereo-aware MFFN + Refinement, and their corresponding adapted versions incorporating the proposed self-supervised real adaptation strategy. This evaluation demonstrates the effectiveness of adaptation and enables comparison with prior pose estimation approaches in surgical robotics.

A. Performance with and without Self-Supervised Adaptation

As described in Section VII-B, the proposed self-supervised real adaptation framework constructs pseudo ground-truth supervision from real observations. Using only 150 pseudo GT samples—distinct from the validation set—and fine-tuning only the pose regression heads of the MFFN and refinement module, substantial bias reduction is achieved, as visualized in Fig. 10.

Quantitative results over the 1,000 real-world samples are summarized in Table V. For the MFFN model, translation error is reduced from 3.69 mm to 1.57 mm, corresponding to a 57.5% improvement, while rotation error decreases from

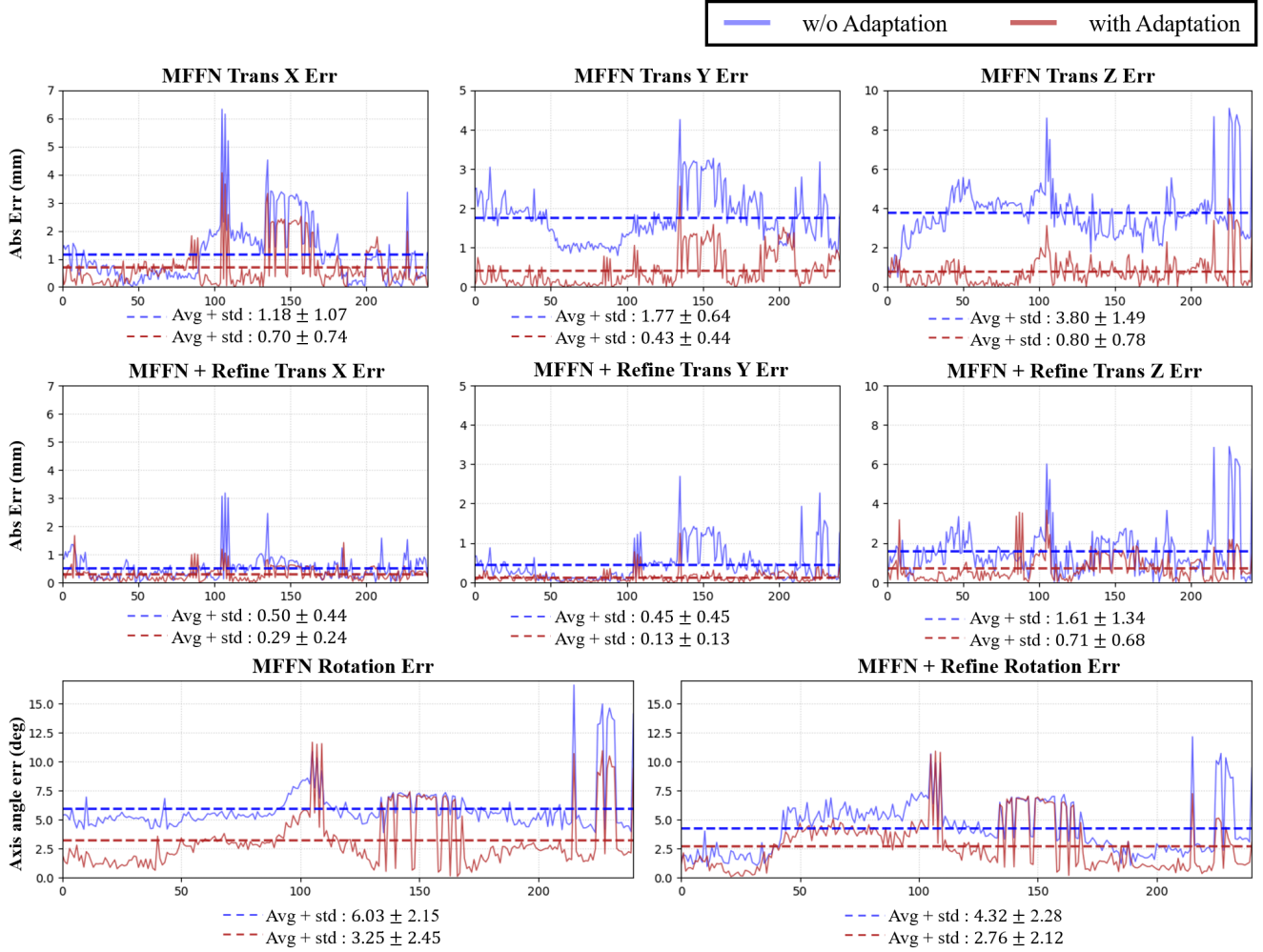


Fig. 10: Axis-wise TCP translation errors (x, y, z) and rotation error magnitude over 250 joint configurations, comparing performance before (blue) and after (red) self-supervised adaptation. (Top row) MFFN only. (Bottom row) MFFN + Refinement. Dashed lines indicate mean values. Adaptation consistently reduces bias across all axes, with the most pronounced improvement along the z-axis (depth direction).

TABLE V: Pose estimation performance comparison on the proposed model with and without adaption. The validation has been performed on the real environments with 1000 joint configurations.

Method	Trans. Error [mm]	Rot. Error [deg]
MFFN (w/o adapt)	3.69 ± 1.30	7.10 ± 1.91
MFFN + Refine(w/o adapt)	1.68 ± 0.97	4.82 ± 2.25
MFFN (Adapt)	1.57 ± 1.20	3.86 ± 2.00
MFFN + Refine (Adapt)	0.83 ± 0.70	2.76 ± 1.74

7.10° to 3.86° (45.6% improvement).

For the MFFN + Refinement framework, translation error decreases from 1.68 mm to 0.83 mm (50.6% improvement), and rotation error from 4.82° to 2.76° (42.7% improvement).

Overall, self-supervised adaptation achieves approximately 50% error reduction in both translation and rotation using a small set of pseudo GT samples. These results demonstrate that the proposed adaptation strategy effectively compensates for extrinsic calibration bias by aligning pose estimates with the model’s learned visual geometric representations, without requiring manual annotation.

B. Performance Comparison with Previous State-of-the-Art Methods

We evaluate the proposed model with self-supervised adaptation (Section VII-B) in real-world environments and compare it with prior state-of-the-art methods in Table VI. Qualitative results on real-world data, including predicted keypoints, segmentation masks, and 6D pose estimates, are presented in Fig. 11. The method of Zhou *et al.* [15] represents the previous leading performance for continuum manipulator pose estimation.

Their feed-forward baseline, which relies solely on segmentation masks, achieves a translation error of 1.64 mm and a rotation error of approximately 5.0° . When combined with iterative render-and-compare refinement, the error is reduced to 1.24 mm and 3.2° for translation and rotation, respectively, at the cost of substantially increased inference time.

In contrast, our stereo-based MFFN achieves 1.57 mm translation error and 3.86° rotation error after sim-to-real adaptation, without iterative optimization. When coupled with the proposed feed-forward rendering refinement mod-

TABLE VI: **Quantitative comparison of real-world TCP pose estimation performance with prior state-of-the-art methods.** Translation and rotation errors are reported together with sensing modality, inference time, camera configuration, platform, and pose annotation strategy.

Method	Trans. Err [mm]	Rot. Err [deg]	Inf. Time [ms]	Val. Size	Modality	Platform	Validation GT
Zhou et al. (base) [15]	1.64 ± 0.77	5.02 ± 1.97	17	162	Single (mask)	Continuum	Marker
Zhou et al. (refine) [15]	1.24 ± 0.85	3.20 ± 1.45	849	162	Single (mask)	Continuum	Marker
Ye et al. [17]	3.14 ± 1.96	6.88 ± 4.58	34.5	1000	Single (kpts)	dVRK	Manual
Allan et al. [18]	3.85 ± 3.64	24.64 ± 14.90	3k–6k	1000	Single (mask)	dVRK	Manual
MFFN (Adapt)	1.57 ± 1.20	3.86 ± 2.00	143	1000	Multi	Continuum	Marker
MFFN + Refine (Adapt)	0.83 ± 0.70	2.76 ± 1.74	180	1000	Multi	Continuum	Marker

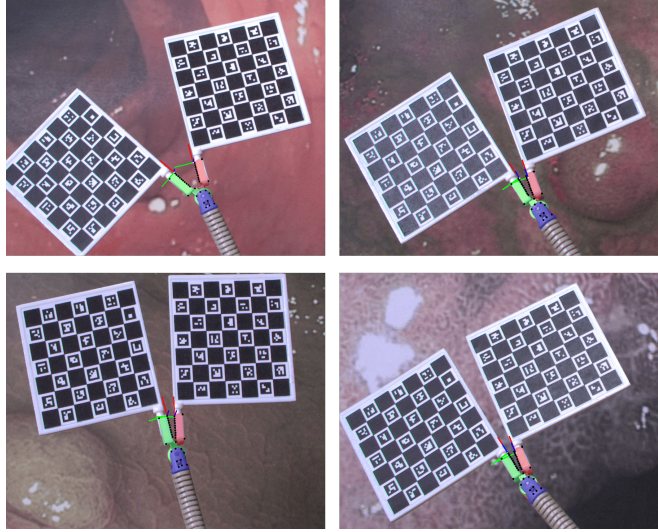


Fig. 11: Real-world validation results. Predicted segmentation masks, keypoints, and 6-DoF poses are overlaid on real stereo images. The estimated pose from the proposed model is visualized as coordinate axes attached to the manipulator, demonstrating accurate alignment between the predicted geometric representation and real observations under diverse viewpoints and background conditions.

ule, performance further improves to 0.83 mm and 2.76° , corresponding to relative improvements of 34.6% in translation and 13.8% in rotation over the previous state of the art, while reducing inference time from 849 ms to 180 ms.

Notably, the MFFN alone already achieves performance comparable to the iterative refinement approach of Zhou *et al.*, which we attribute to the integration of complementary geometric cues, including bounding boxes, segmentation masks, keypoints, and heatmaps. In contrast, prior work relies on a single-modality mask-based representation, which is more susceptible to segmentation failures. Furthermore, while Zhou *et al.* evaluate on only 162 test samples, our method is validated on over 1,000 randomized real-world trajectories captured under four distinct endoscopic imaging conditions, demonstrating improved generalization.

We also outperform earlier vision-based pose estimation approaches evaluated on the dVRK platform [17], [22], where ground-truth validation poses are obtained through manual annotation of image observations. While this enables practical dataset construction, such human-in-the-loop labeling inherently limits geometric precision compared to marker-based pose measurement. Moreover, these methods

report translation errors exceeding 3 mm, indicating substantially lower pose estimation accuracy.

IX. CLOSED-LOOP CONTROL OF THE CONTINUUM MANIPULATOR

This section presents the position-based visual servoing (PBVS) framework driven by the estimated TCP pose in real-world environments. Closed-loop control performance is evaluated through two representative tasks: (i) repeated single-point reaching experiments to assess convergence accuracy and repeatability, with marker-based visual servoing serving as an upper-bound baseline; and (ii) continuous box-shaped trajectory tracking tests comparing open-loop control, marker-based servoing, and the proposed model-driven visual servoing. Here, model-driven visual servoing refers to closed-loop control using the TCP pose estimated by the proposed adapted MFFN+refinement network.

A. Jacobian-Based Position-Based Visual Servoing

At each control cycle k , the TCP pose is obtained in the camera frame either from the proposed markerless estimator or from a Charuco marker-based tracking system. Using calibrated hand–eye extrinsics, the observed pose is transformed into the robot base frame as

$${}^{base}\mathbf{T}_{tcp,k}^{obs} = {}^{base}\mathbf{T}_{cam} {}^{cam}\mathbf{T}_{tcp,k}^{obs}. \quad (53)$$

The corresponding joint configuration is recovered through inverse kinematics:

$$\mathbf{q}_k = \text{IK}({}^{base}\mathbf{T}_{tcp,k}^{obs}), \quad (54)$$

and the geometric Jacobian $\mathbf{J}(\mathbf{q}_k)$ is evaluated at the current configuration.

Let ${}^{base}\mathbf{T}_{tcp}^*$ denote the desired target pose. The relative pose error is computed as

$$\mathbf{T}_{err,k} = ({}^{base}\mathbf{T}_{tcp,k}^{obs})^{-1} {}^{base}\mathbf{T}_{tcp}^*. \quad (55)$$

The translational and rotational error components expressed in the base frame are defined as

$$\begin{aligned} \mathbf{e}_{p,k} &= {}^{base}\mathbf{R}_{tcp,k} \mathbf{p}_{err,k}, \\ \mathbf{e}_{R,k} &= {}^{base}\mathbf{R}_{tcp,k} \text{rotvec}(\mathbf{R}_{err,k}). \end{aligned} \quad (56)$$

The Cartesian task-space error vector is given by

$$\mathbf{e}_k = \begin{bmatrix} \mathbf{e}_{p,k} \\ \mathbf{e}_{R,k} \end{bmatrix}. \quad (57)$$

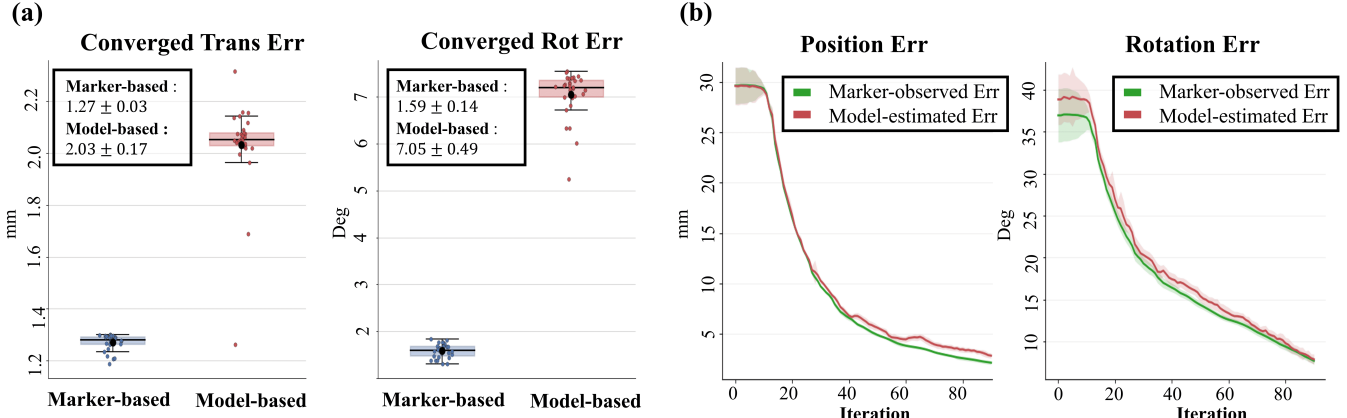


Fig. 12: Visual servoing performance comparison and convergence analysis. (a) Final translational and rotational errors after convergence for marker-based and model-based visual servoing over 30 trials. (b) Convergence behavior during model-based visual servoing. The model-estimated error closely follows the marker-observed ground-truth error, demonstrating that the proposed model provides reliable pose feedback and accurately reflects the true convergence dynamics.

The incremental joint update is computed using the pseudoinverse of the Jacobian:

$$\Delta \mathbf{q}_k = \mathbf{J}(\mathbf{q}_k)^\dagger (\alpha \mathbf{e}_k), \quad (58)$$

where α is a positive scalar gain. In our implementation, we set $\alpha = 0.05$ to ensure stable convergence in the presence of hysteresis, which induces kinematic model mismatch inherent to continuum manipulators.

The joint commands are updated as

$$\mathbf{q}_{k+1} = \mathbf{q}_k + \Delta \mathbf{q}_k, \quad (59)$$

and applied for the next control cycle.

The control loop iterates until the translational or rotational error norm falls below a predefined threshold or a maximum of 500 iterations is reached. Convergence thresholds are first determined using the marker-based servoing baseline, where translation and rotation norms are set to 1 mm and 0.05 rad, respectively.

Based on the real-world pose estimation statistics in Table VI, where the proposed model exhibits a mean translation error of 0.83 mm with 0.7 mm standard deviation and a mean rotation error of 2.76° with 1.74° standard deviation, relaxed thresholds are used for model-driven servoing to account for observation uncertainty. Specifically, convergence is defined as achieving a translational error below 2.5 mm and a rotational error below 0.127 rad, corresponding approximately to the mean estimation error plus two standard deviations. This modality-dependent thresholding ensures a physically meaningful stopping criterion while accommodating the inherent uncertainty of learned pose estimation.

B. Point-Reaching Tasks

To evaluate the repeatability and convergence behavior of the proposed pose-estimation-driven visual servoing, we quantitatively compare closed-loop control performance under two observation modalities: marker-based pose tracking and the proposed markerless pose estimator. Repeated single-point reaching trials are conducted to assess convergence

accuracy and repeatability in both translational and rotational errors.

The detailed numerical results are presented in Fig. 12. For each modality, the manipulator is commanded to reach the same target pose over 30 independent trials. As shown in Fig. 12(a), the marker-based controller converges to a translational error of 1.27 ± 0.03 mm, while the proposed method converges to 2.03 ± 0.17 mm, exhibiting comparable repeatability as reflected by similar standard deviations. For rotational accuracy, marker-based servoing achieves 1.59 ± 0.14 °, whereas the proposed method converges to 7.05 ± 0.49 °, again demonstrating consistent repeatability.

Fig. 12(b) compares the model-estimated pose error and the independently marker-observed error during marker-based servoing across 30 trials. The close agreement in error evolution between the two measurements indicates that the proposed pose estimator accurately captures the true convergence trend of the robot without inducing oscillations or divergence, thereby enabling stable closed-loop control.

To evaluate control efficiency, we additionally compare the average number of iterations and convergence time for both modalities. Marker-based servoing requires 285.87 iterations on average, with a mean convergence time of 38.55 s, corresponding to approximately 0.135 s per iteration. In contrast, model-driven servoing converges in 98 iterations on average with a mean convergence time of 42.24 s, corresponding to approximately 0.431 s per iteration. The longer per-iteration time in the model-driven case is attributed to the computational overhead of pose estimation. The control loop operates at a fixed update interval of 0.05 s, ensuring consistent temporal discretization and stable convergence behavior.

C. Trajectory Tracking Tasks

This section evaluates trajectory-level visual servoing performance under continuous motion. A square-shaped reference trajectory consisting of 127 target poses is generated, and tracking performance is compared across three control

TABLE VII: Quantitative comparison of closed-loop visual servoing performance on trajectory tracking under different control modalities, including markerless position-based visual servoing (ours), marker-based pose feedback, and open-loop control.

Method	Translation Error (mm)	Rotation Error (deg)
Model-based	2.07 ± 0.91	7.41 ± 2.92
Marker-based	1.06 ± 0.27	2.00 ± 0.61
Open-loop	13.74 ± 5.67	18.00 ± 7.50

modalities: open-loop control, marker-based visual servoing, and the proposed model-driven visual servoing.

Quantitative results are summarized in Table VII. The proposed model-driven servoing achieves a mean translation error of 2.07 ± 0.91 mm and a mean rotation error of $7.41 \pm 2.92^\circ$, representing substantial improvements over open-loop control, which exhibits 13.74 ± 5.67 mm translational error and $18.00 \pm 7.50^\circ$ rotational error. This corresponds to an approximately 85% reduction in translation error and a 59% reduction in rotation error relative to open-loop operation.

Compared with marker-based visual servoing, which achieves 1.06 ± 0.27 mm translation error and $2.00 \pm 0.61^\circ$ rotation error, the proposed method shows only a modest performance gap of 1.01 mm in translation and 5.41° in rotation. Despite operating without physical markers, the proposed controller attains trajectory tracking accuracy approaching that of marker-based servoing.

Fig. 13 visualizes the 3D trajectory tracking behavior. While the model-driven servoing exhibits minor transient deviations, the end-effector consistently converges toward the desired trajectory. Marker-based servoing closely follows the reference path with minimal deviation, whereas open-loop control fails to track the trajectory and diverges significantly from the target.

Notably, the proposed controller employs a basic Jacobian-based pose-based visual servoing (PBVS) formulation. Further improvements are expected through the integration of advanced control strategies, such as adaptive or model-predictive schemes, indicating strong potential for future closed-loop refinement.

In addition, the achieved 2 millimeter-level trajectory tracking accuracy aligns with clinically relevant scales of endoscopic lesion manipulation. Colorectal polyps are commonly categorized as diminutive (≤ 5 mm), small (6–9 mm), and large (≥ 10 mm) in clinical practice [38]. The proposed closed-loop control accuracy therefore enables precise positioning even for diminutive lesions, highlighting the practical applicability of the proposed markerless visual servoing framework in real endoscopic scenarios.

X. CONCLUSION

This paper presented a unified framework for markerless stereo 6D pose estimation and closed-loop control of continuum manipulators. Existing vision-based approaches for continuum manipulators suffer from three primary limitations: (i) the lack of photo-realistic simulators capable of generating pixel-accurate annotations, (ii) limited exploitation of geometric cues, often relying on single-modality features and

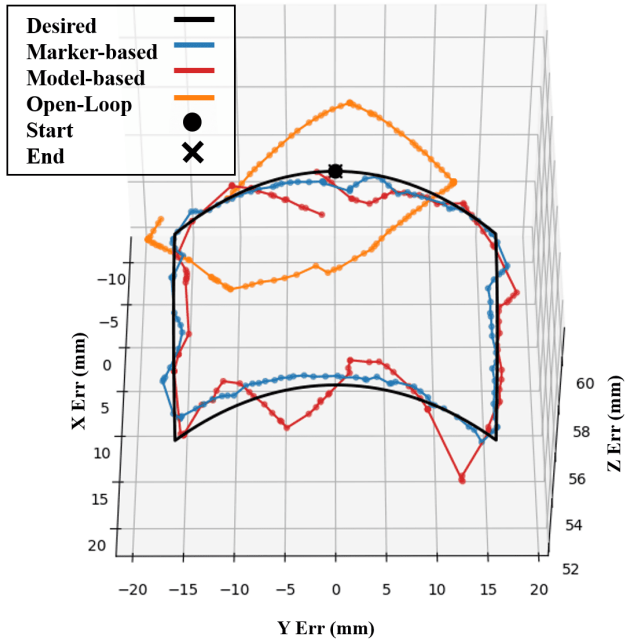


Fig. 13: Comparison of square-shaped trajectory tracking performance. The desired trajectory (black) is tracked using marker-based visual servoing (blue), model-based visual servoing (red), and open-loop control (orange). The proposed model-based servoing achieves accurate trajectory tracking without marker feedback and closely follows the marker-based servoing performance, while open-loop control exhibits substantial tracking errors. Start and end points are indicated by \bullet and \times , respectively.

monocular imagery, and (iii) high computational overhead in iterative render-and-compare pipelines, which restricts their applicability to real-time position-based visual servoing.

To address these limitations, we first developed a photo-realistic simulation pipeline that enables large-scale automatic dataset generation with physically plausible motion under rigid-body constraints together with precise mask, keypoint, and pose annotations. We then introduced a stereo-aware multi-feature fusion network that jointly leverages segmentation masks, keypoints, heatmaps, and bounding boxes to enhance geometric observability. To enforce geometric consistency without iterative optimization, we proposed a feed-forward rendering-based refinement module that predicts residual pose corrections in a single pass. On synthetic data, the proposed method achieves translation and rotation errors of 0.14 mm and 0.44° , respectively, representing approximately 70% improvement over a monocular baseline.

Furthermore, we introduced a self-supervised sim-to-real adaptation strategy based on pseudo ground-truth refinement, reducing real-world pose error by approximately 50% using only 150 unlabeled images. Extensive real-world experiments demonstrate a mean translation error of 0.83 mm and a mean rotation error of 2.76° , corresponding to 34.6% and 13.8% improvements over prior state-of-the-art methods.

Finally, we validated fully markerless closed-loop visual servoing driven solely by the estimated 6D pose. In repeated point-reaching experiments, the proposed controller achieved high repeatability, with translation and rotation standard deviations of 0.17 mm and 0.49° , respectively. In square-shaped

trajectory tracking tasks, the model-driven servoing achieved a mean translation error of 2.07 ± 0.91 mm and a mean rotation error of $7.41 \pm 2.92^\circ$, corresponding to 85% and 59% reductions in translation and rotation errors compared to open-loop control. These results demonstrate that accurate markerless pose estimation can directly enable stable and clinically relevant closed-loop control performance.

Despite these advances, several limitations remain. First, performance under severe occlusions caused by tissue, instruments, or surgical smoke has not yet been fully addressed. Second, the current Jacobian-based PBVS formulation does not explicitly model nonlinearities induced by hysteresis, suggesting that advanced control strategies such as adaptive or model-predictive control may further improve tracking accuracy. Finally, although the proposed framework significantly reduces inference time compared to prior render-and-compare approaches (1000ms), the current runtime of 210 ms per frame remains a constraint for high-frequency real-time deployment and warrants further optimization.

Overall, this work demonstrates that physics-grounded simulation, multi-feature stereo fusion, and feed-forward geometric refinement can collectively enable accurate and practical markerless closed-loop control of continuum manipulators.

REFERENCES

- [1] M. Hwang and D. S. Kwon, "K-FLEX: A flexible robotic platform for scar-free endoscopic surgery," *Int. J. Med. Robot. Comput. Assist. Surg.*, vol. 16, 2020.
- [2] M. Remacle *et al.*, "Transoral robotic surgery (TORS) with the Medrobotics Flex™ System: first surgical application on humans," *Eur. Arch. Oto-Rhino-Laryngol.*, vol. 272, pp. 1451–1455, 2015.
- [3] S. J. Phee *et al.*, "Master and slave transluminal endoscopic robot (MASTER) for natural Orifice Transluminal Endoscopic Surgery (NOTES)," in *Proc. Annu. Int. Conf. IEEE Eng. Med. Biol. Soc.*, 2009, pp. 1192–1195.
- [4] L. Zorn *et al.*, "A Novel Telemanipulated Robotic Assistant for Surgical Endoscopy: Preclinical Application to ESD," *IEEE Trans. Biomed. Eng.*, vol. 65, pp. 797–808, 2018.
- [5] J. Park *et al.*, "Sam: Semi-active mechanism for extensible continuum manipulator and real-time hysteresis compensation control algorithm," *Int. J. Med. Robot. Comput. Assist. Surg.*, vol. 20, 2024.
- [6] M. M. Dalvand *et al.*, "An analytical loading model for n -tendon continuum robots," *IEEE Trans. Robot.*, vol. 34, pp. 1215–1225, 2018.
- [7] D. Ji *et al.*, "Analysis of twist deformation in wire-driven continuum surgical robot," *Int. J. Control. Autom. Syst.*, vol. 18, pp. 10–20, 2020.
- [8] D. Kim *et al.*, "Recurrent neural network with preisach model for configuration-specific hysteresis modeling of tendon-sheath mechanism," *IEEE Robot. Autom. Lett.*, vol. PP, pp. 1–1, 2022.
- [9] R. Roy *et al.*, "Modeling and estimation of friction, extension, and coupling effects in multisegment continuum robots," *IEEE/ASME Trans. Mech.*, vol. 22, pp. 909–920, 2017.
- [10] J. Park *et al.*, "Hysteresis compensation of flexible continuum manipulator using rgbd sensing and temporal convolutional network," *IEEE Robotics and Automation Letters*, vol. 9, pp. 6091–6098, 2024.
- [11] Y. Chitalia *et al.*, "Towards fbg-based shape sensing for micro-scale and meso-scale continuum robots with large deflection," *IEEE Robotics and Automation Letters*, 2020.
- [12] F. Khan *et al.*, "Pose measurement of flexible medical instruments using fiber bragg gratings in multi-core fiber," *IEEE Sensors Journal*, vol. 20, no. 23, pp. 14 009–14 018, 2020.
- [13] P. Kazanzides *et al.*, "An open-source research kit for the Da Vinci surgical system," in *Proc. IEEE Int. Conf. Robot. Autom.*, 2014, p. 6434–6439.
- [14] Y. Ma and J. Burgner-Kahrs, "Learning-based pose estimation for continuum surgical instruments using monocular images," *IEEE Robotics and Automation Letters*, vol. 6, no. 2, pp. 2709–2716, 2021.
- [15] C. Zhou *et al.*, "A markerless 3d tracking framework for continuum surgical tools using a surgical tool partial pose estimation network based on domain randomization," *Advanced Intelligent Systems*, vol. 6, no. 4, p. 2300434, 2024.
- [16] L. Wang *et al.*, "Vision-based markerless tracking for continuum surgical instruments in robot-assisted minimally invasive surgery," *IEEE Robotics and Automation Letters*, vol. 8, 2023.
- [17] M. Ye *et al.*, *Real-Time 3D Tracking of Articulated Tools for Robotic Surgery*. Springer International Publishing, 2016, p. 386–394.
- [18] M. Allan *et al.*, "3-d pose estimation of articulated instruments in robotic minimally invasive surgery," *IEEE Transactions on Medical Imaging*, vol. 37, no. 5, pp. 1204–1213, 2018.
- [19] Z. Zhao *et al.*, "Tracking-by-detection of surgical instruments in minimally invasive surgery via the convolutional neural network deep learning-based method," *Computer Assisted Surgery*, vol. 22, pp. 26–35, 2017.
- [20] A. Reiter *et al.*, "Learning-based segmentation of multi-jointed robotic arms in surgical video," *International journal of computer assisted radiology and surgery*, vol. 9, pp. 37–46, 2014.
- [21] R. Spektor *et al.*, "Monocular pose estimation of articulated surgical instruments in open surgery," *arXiv preprint arXiv:2407.12138*, 2024.
- [22] M. Allan *et al.*, "2017 robotic instrument segmentation challenge," *International Journal of Computer Assisted Radiology and Surgery*, vol. 14, pp. 1601–1610, 2019.
- [23] B. Wu *et al.*, "Closed-loop pose control and automated suturing of continuum surgical manipulators with customized wrist markers under stereo vision," *IEEE Robotics and Automation Letters*, vol. 6, no. 4, pp. 7137–7144, 2021.
- [24] I. Abdulhafiz *et al.*, "Deep direct visual servoing of tendon-driven continuum robots," in *2022 IEEE 18th International Conference on Automation Science and Engineering (CASE)*, 2022, p. 1977–1984.
- [25] J. Burgner-Kahrs *et al.*, "Continuum robots for medical applications: A survey," *IEEE Transactions on Robotics*, 2015.
- [26] C. Shi *et al.*, "Shape sensing techniques for continuum robots in minimally invasive surgery: A survey," *IEEE Transactions on Biomedical Engineering*, vol. 64, no. 8, pp. 1665–1678, 2017.
- [27] M. Mittal *et al.*, "Orbit: A unified simulation framework for interactive robot learning environments," *IEEE Robotics and Automation Letters*, vol. 8, no. 6, p. 3740–3747, Jun. 2023. [Online]. Available: <http://dx.doi.org/10.1109/LRA.2023.3270034>
- [28] Q. Yu *et al.*, "Orbit-surgical: An open-simulation framework for learning surgical augmented dexterity," 2024. [Online]. Available: <https://arxiv.org/abs/2404.16027>
- [29] Z. Liang *et al.*, "Differentiable rendering-based pose estimation for surgical robotic instruments," in *2025 IEEE/RSJ International Conference on Intelligent Robots and Systems (IROS)*, 2025, pp. 20 898–20 905.
- [30] J. Lu *et al.*, "Ctrnet-x: Camera-to-robot pose estimation in real-world conditions using a single camera," in *IEEE International Conference on Robotics and Automation (ICRA)*. IEEE, 2025, pp. 1914–1920.
- [31] Y. Li, G. Wang, and X. Ji, "Deepim: Deep iterative matching for 6d pose estimation," in *Proceedings of the European Conference on Computer Vision (ECCV)*, 2018.
- [32] "Closed-loop control of soft continuum manipulators under tip follower actuation," *The International Journal of Robotics Research*, vol. 40, no. 6-7, pp. 923–938, 2021.
- [33] M. C. Yip and D. B. Camarillo, "Model-less feedback control of continuum manipulators in constrained environments," *IEEE Transactions on Robotics*, vol. 30, no. 4, pp. 880–889, 2014.
- [34] T. G. Thuruthel *et al.*, "Model-based reinforcement learning for closed-loop dynamic control of soft robotic manipulators," *IEEE Transactions on Robotics*, vol. 35, no. 1, pp. 124–134, 2019.
- [35] M. Ye *et al.*, "Online tracking and retargeting with applications to optical biopsy in gastrointestinal endoscopic examinations," *Medical Image Analysis*, vol. 30, pp. 144–157, 2016.
- [36] S. Levine, C. Finn, T. Darrell, and P. Abbeel, "End-to-end training of deep visuomotor policies," *Journal of Machine Learning Research*, vol. 17, pp. 1–40, 2016.
- [37] M. A. Fischler and R. C. Bolles, "Random sample consensus: a paradigm for model fitting with applications to image analysis and automated cartography," *Commu. of the ACM*, vol. 24, pp. 381 – 395, 1981.
- [38] T. Kaltenbach *et al.*, "Endoscopic removal of colorectal lesions—recommendations by the US multi-society task force on col-

orectal cancer," *Gastroenterology*, vol. 158, no. 4, pp. 1095–1129, 2020.